

Reconciling volcanic deformation, degassing and petrological data using thermodynamic models

Stanley Tze Hou Yip¹, Juliet Biggs², Marie Edmonds³, Philippa Liggins³, and Oliver Shorttle³

¹University of Bristol

²University of Bristol, UK

³University of Cambridge

November 26, 2022

Abstract

Two of the most widely observed co-eruptive volcanic phenomena - ground deformation and volcanic outgassing - are fundamentally linked via the mechanism of magma degassing and the development of compressibility, which controls how the volume of magma changes in response to a change in pressure. Here we use thermodynamic models (constrained by petrological data) to reconstruct volatile exsolution and the consequent changes in magma properties. Co-eruptive SO₂ degassing fluxes may be predicted from the mole fraction of exsolved SO₂ that develops in magma whilst stored prior to eruption and during decompression. Co-eruptive surface deformation may be predicted given estimates of erupted volume and the ratio between chamber compressibility and magma compressibility. We conduct sensitivity tests to assess how varying magma volatile content, crustal properties, and chamber geometry may affect co-eruptive deformation and degassing. We find that magmatic H₂O content has the most impact on both SO₂ flux and volume change (normalised for erupted volumes). Our findings have general implications for typical arc and ocean island volcanic systems. The higher magmatic water content of arc basalts leads to a high pre-eruptive exsolved volatile content, making the magma more compressible than ocean island eruptions. Syn-eruptive gas fluxes are overall higher for arc eruptions, although SO₂ fluxes are similar for both settings (SO₂ flux for ocean island basalt eruptions is dominated by decompressional degassing). Our models are consistent with observation: deformation has been detected at 48% of ocean island eruptions (16/33) during the satellite era (2005-2020), but only 11% of arc basalt eruptions (7/61).

1 **Reconciling volcanic deformation, degassing and**
2 **petrological data using thermodynamic models**

3 **Stanley Tze Hou Yip^{1,2}, Juliet Biggs^{1,2}, Marie Edmonds^{1,3}, Philippa Liggins³,**
4 **Oliver Shorttle³**

5 ¹Centre for the Observation and Modelling of Earthquakes, Volcanoes and Tectonics (COMET)

6 ²School of Earth Sciences, University of Bristol, Wills Memorial Building, Bristol, BS8 1RJ, United

7 Kingdom

8 ³Department of Earth Sciences, University of Cambridge, Cambridge, CB2 3EQ, United Kingdom

9 **Key Points:**

- 10 • We use petrological data and a thermodynamic framework to model volcanic de-
11 formation and SO₂ degassing.
- 12 • High magmatic volatile content of arc basalts contributes to the lack of deforma-
13 tion observed at arc basalt eruptions.

Corresponding author: Stanley Tze Hou Yip, stanley.th.yip@bristol.ac.uk

Abstract

Two of the most widely observed co-eruptive volcanic phenomena - ground deformation and volcanic outgassing - are fundamentally linked via the mechanism of magma degassing and the development of compressibility, which controls how the volume of magma changes in response to a change in pressure. Here we use thermodynamic models (constrained by petrological data) to reconstruct volatile exsolution and the consequent changes in magma properties. Co-eruptive SO_2 degassing fluxes may be predicted from the mole fraction of exsolved SO_2 that develops in magma whilst stored prior to eruption and during decompression. Co-eruptive surface deformation may be predicted given estimates of erupted volume and the ratio between chamber compressibility and magma compressibility. We conduct sensitivity tests to assess how varying magma volatile content, crustal properties, and chamber geometry affect co-eruptive deformation and degassing. We find that magmatic H_2O content has the most impact on both SO_2 flux and volume change (normalised for erupted volumes). Our findings have general implications for typical arc and ocean island volcanic systems. The higher magmatic water content of arc basalts leads to a high pre-eruptive exsolved volatile content, making the magma more compressible than ocean island eruptions. Syn-eruptive gas fluxes are overall higher for arc eruptions, although SO_2 fluxes are similar for both settings (SO_2 flux for ocean island basalt eruptions is dominated by decompressional degassing). Our models are consistent with observation: deformation has been detected at 48% of ocean island eruptions (16/33) during the satellite era (2005-2020), but only 11% of arc basalt eruptions (7/61).

Plain Language Summary

Volcano monitoring provides a wealth of data upon which to base activity forecasts, yet we lack quantitative models to integrate two of the most widely observed eruptive parameters: ground deformation and volcanic gas fluxes. When magma exsolves volatiles (water, carbon dioxide, sulfur) during storage in the crust prior to eruptions, the fluid bubbles cause the magma to become compressible, and behave like a sponge. The effect of this degassing is that when pressure changes in the magma chamber (due to eruption, or due to recharge), the gas bubbles expand or contract in response, effectively maintaining a near-constant volume for the magma. Understanding the effect of magmatic gas on volume changes is key to developing integrated, satellite-based volcano monitoring approaches.

1 Introduction

The increasing number of satellite missions launched in the past decade has driven an explosion in data for studying the Earth's dynamic processes (Chaussard et al., 2013; Morales Rivera et al., 2016; Carn et al., 2017; Furtney et al., 2018; Biggs & Wright, 2020). The array of sensors onboard satellites routinely provides near real-time observations of volcanic eruptions such as SO₂ plumes and clouds (e.g., Carn et al., 2016; Carboni et al., 2016; Ge et al., 2016) and ground deformation (e.g., Biggs & Pritchard, 2017; Ebmeier et al., 2018; Pritchard et al., 2018), both of which are key indicators of eruption progress and may be used to track eruptive activity and understand pre-eruptive magma storage conditions. However, observations show that not all volcanoes exhibit pre- or co-eruptive deformation (Rivalta & Segall, 2008; Biggs et al., 2014; Reath et al., 2020); the causes of the wide variation in deformation systematics between volcanoes and between tectonic settings are not well understood (Piochi et al., 2005; Ebmeier et al., 2013b; Chaussard & Amelung, 2014). Reconciling observations of volcanic deformation and degassing can help identify the conditions that lead to the lack of observations of ground deformation (Kilbride et al., 2016; Reath et al., 2020). The magmatic processes that drive volcanic deformation and degassing are fundamentally linked: exsolution of volatiles from silicate melt in crustal magma reservoirs (during second boiling or due to decompression) causes magma to become compressible, fundamentally changing the volume-change response to pressure perturbations experienced by the magma during eruption and recharge (Woods & Huppert, 2003; Kilbride et al., 2016; Wong et al., 2017; Wong & Segall, 2020). However, while it is becoming increasingly common to compile multisensor data (e.g., Furtney et al., 2018; Reath et al., 2019, 2020), until recently there has not been a quantitative framework to jointly interpret observations of volcanic deformation and degassing, including CO₂ and SO₂ gas fluxes (Girona et al., 2014; Kilbride et al., 2016; Wong & Segall, 2020).

Thermodynamic models, constrained by petrological data, may be used to calculate the varying proportions of melt, crystals and exsolved volatiles in shallow magmatic reservoirs under a range of pressure, temperature and magma composition conditions (e.g., Papale et al., 2006; Gualda et al., 2012; Burgisser et al., 2015; Liggins et al., 2020, 2021). The exsolved volatile phase generated both during crystallisation and second boiling in the reservoir, and during decompressional degassing, contributes to the mass of gases released prior to and during an eruption (Wallace & Carmichael, 1992; Wallace,

2005). Since the physicochemical properties of magmas are interdependent, magma prop-
erties such as density and compressibility can be calculated using the law of conserva-
tion of mass (Spera, 2000; Huppert & Woods, 2002). The compressibility of magma and
its surrounding host rock controls the co-eruptive volume change of magma chambers,
which consequently affects co-eruptive ground deformation at the surface (e.g., Huppert
& Woods, 2002; Edmonds et al., 2019; Head et al., 2019; Sigmundsson et al., 2020).

Previous work by Kilbride et al. (2016) introduced a thermodynamic framework
for reconciling satellite observations of atmospheric sulfur yield and volcanic deforma-
tion during discrete explosive eruptions (where there is assumed to be little volatile ex-
solution during magma ascent). The framework uses thermodynamic models to illustrate
the effect of initial magmatic volatile content (H_2O , CO_2) and oxygen fugacity on SO_2
degassing and volcanic deformation (Kilbride et al., 2016). Kilbride et al. (2016) then
compared their model predictions to observations from 11 discrete explosive eruptions
to illustrate the factors controlling volcanic deformation and degassing (Kilbride et al.,
2016).

This study extends the thermodynamic framework developed by Kilbride et al. (2016)
to enable large-scale analyses, such as sensitivity tests and Monte-Carlo simulations, across
a wider range of magma compositions and eruption styles. The sensitivity tests for magma
of basaltic composition explore how varying initial magmatic volatile contents (H_2O , CO_2 ,
S) and oxygen fugacity affect magma properties and consequently volcanic deformation
and degassing. We also consider the effects of variable crustal shear modulus μ and cham-
ber geometry on co-eruptive volcanic deformation. Finally, we compare the properties
of arc and ocean island magmas arising from their different volatile contents and discuss
the implications for satellite observations of deformation and degassing during eruptions
in different tectonic settings.

2 Background: Observations Of Volcanic Deformation and Degassing

Satellites with short repeat time and high spatial resolution provide consistent spatio-
temporal coverage for monitoring volcanoes on regional to global scales (e.g., TerraSAR-
X, Sentinel-1), which is particularly valuable for monitoring volcanoes with few or no
ground-based stations (e.g., Telling et al., 2015; Carboni et al., 2016; Ebmeier et al., 2016;
Delgado et al., 2017; Pritchard et al., 2018; Coppola et al., 2020). Interferometric Syn-
thetic Aperture Radar (InSAR) is a satellite technique that measures the phase change

111 between pairs of satellite radar images to generate maps of surface displacement, which
112 may be used to monitor volcanoes exhibiting deformation in response to changes in magma
113 activity . However, while many volcanoes exhibit pre-eruptive inflation associated with
114 magma intrusion and/or co-eruptive deflation during magma withdrawal, some do not
115 (Moran et al., 2006; Rivalta & Segall, 2008; Biggs & Pritchard, 2017; Ebmeier et al., 2018).
116 One of the possible reasons is due to the presence of an exsolved gas phase that is more
117 compressible than the surrounding crust and silicate melt (Huppert & Woods, 2002; Woods
118 & Huppert, 2003; Kilbride et al., 2016).

119 The most volumetrically significant volcanic volatile species produced during an
120 eruption are H_2O and CO_2 , yet it is difficult to distinguish these volatiles from atmo-
121 spheric background in satellite measurements. In contrast, volcanic SO_2 has a strong ab-
122 sorption signal in the near-ultraviolet and infrared spectrum, and thus can be measured
123 using satellite-based spectrometers (e.g., Carn et al., 2016; Carboni et al., 2016).

124 Conceptual models of magmatic systems may be used to understand different de-
125 gassing configurations and their impact on monitoring signals (Figure 1). Volatiles are
126 more soluble at higher pressures and hence they are largely dissolved in silicate melt in
127 deep magmatic systems (Figure 1a). Volatiles exsolve during magma decompression, but
128 if magma stalls in a chamber and cools, volatiles also exsolve during isobaric cooling and
129 crystallisation, a process termed ‘second boiling’ (Edmonds et al., 2019).

130 For an explosive eruption, the high magma ascent rate limits volatile exsolution
131 between the chamber and the surface (Figure 1b) and we make the simplifying assump-
132 tion here that the gas emitted during the eruption is sourced entirely from the pre-eruptive
133 exsolved volatile phase (Wallace & Gerlach, 1994; Wallace, 2005). In this case the amount
134 of gases released (per unit of magma erupted) may be used to constrain the compress-
135 ibility of the magma in the chamber prior to eruption, which will be related to the amount
136 of deformation observed. In contrast, effusive eruptions involve a low magma ascent rate,
137 such that volatiles exsolve extensively in the conduit (Figure 1c). In this case, the gases
138 released during eruptions are mostly produced during magma ascent and cannot sim-
139 ply be related to the compressibility of the magma in the chamber prior to eruption with-
140 out careful reconstruction of the degassing process using a thermodynamic model.

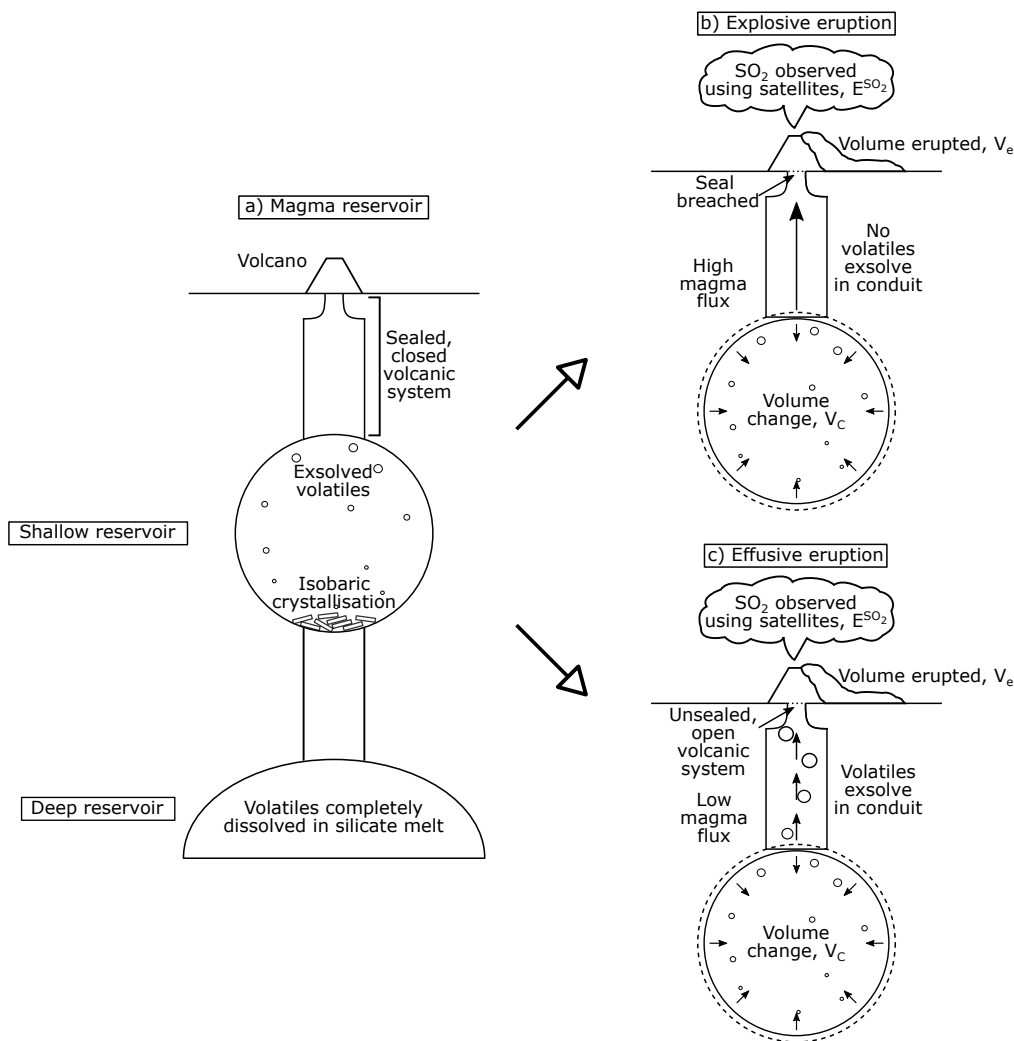


Figure 1. Conceptual model of magma degassing during eruptions of different styles. (a) Volcano with chambers at different depths, prior to an eruption. Magmatic volatiles are more soluble in deep magmatic chambers and thus a higher proportion of the total volatile load will be dissolved in the silicate melt. In the shallow chamber (at a lower pressure) there is a higher proportion of exsolved volatiles, with degassing being driven both by decompression as magma moves up from the lower chamber, and by crystallisation. (b) During explosive eruptions, magma is removed from the chamber and decompressed rapidly, with little volatile exsolution during magma ascent. Much of the volatiles emitted as gases during the eruption represents a pre-eruptive exsolved volatile phase that was present in the chamber prior to decompression (and which made the magma compressible). In this ‘explosive’ case we expect the volume change inferred from ground deformation at the surface to be related to the amount of volatiles emitted during eruption (both normalised by erupted volume). (c) Effusive eruptions, on the other hand, are characterised by a low magma ascent rate between the chamber and the surface, allowing extensive volatile exsolution in the conduit, i.e., co-eruptive degassing. The volcanic gases observed at the surface are mostly derived from decompressional degassing and do not constrain the compressibility of the chamber. In this ‘effusive’ case, we do not expect a relationship between the amount of gases released during the eruption and the volume change inferred for the ‘source’ chamber during eruption.

141 3 Methodology

142 3.1 Thermodynamic modelling

143 Volatile solubility can be defined as the concentration of a volatile species that may
 144 be dissolved in magma at a particular set of pressure, temperature, melt composition and
 145 oxygen fugacity conditions (e.g., Scaillet & Pichavant, 2005; Duan, 2014; Burgisser et
 146 al., 2015). At equilibrium, the fugacity of each volatile species in the melt is equal to its
 147 fugacity in the fluid (Scaillet & Pichavant, 2005), such that a fraction of volatiles are dis-
 148 solved in magma and the remainder are exsolved in the exsolved phase. Since magmatic
 149 volatiles are less soluble at low pressure, magma decompression is a principal driver for
 150 volatile exsolution (e.g., Papale, 1999; Duan, 2014; Burgisser et al., 2015).

151 Thermodynamic models based on mass balance and equilibrium constants may be
 152 used to calculate the mass and composition of the exsolved volatile phase and this may
 153 be then used to estimate bulk magma properties such as density and compressibility (Ohmoto
 154 & Kerrick, 1977; Gaillard & Scaillet, 2014). The concentration of each volatile species
 155 exsolved at any given pressure and temperature can be calculated using its correspond-
 156 ing solubility laws (e.g., Burgisser et al., 2015). Here, we use the Python implementa-
 157 tion of EVo (Liggins et al., 2020, 2021) to predict the physicochemical properties of basaltic
 158 magma, such as the composition of the gas phase and magma density, as a function of
 159 melt composition, magmatic volatile content, oxygen fugacity of magma, temperature
 160 and pressure.

161 We use EVo to calculate magma and fluid compositions in the C-O-H-S-Fe system
 162 during magma decompression (Liggins et al., 2020, 2021). We initialise the model us-
 163 ing the weight fraction of the volatile species H₂O, CO₂ and S as input parameters. The
 164 oxygen fugacity (f_{O_2}) is adjusted relative to the Ni-NiO buffer (NNO). EVo can be ini-
 165 tialised by either 1) specifying starting pressure (p), and gas weight fraction (w_g), or 2)
 166 calculating the saturation pressure for the given composition (i.e., $w_g \approx 0$ wt%). Here
 167 we use the saturation point based on melt composition to find an appropriate starting
 168 pressure/depth (Liggins et al., 2021).

169 At a specified depth, the gas volume fraction (V_g) is controlled by the total gas weight
 170 fraction (w_g) and gas density (ρ_g):

$$171 V_g = \left(1 + \frac{MP(1 - w_g)}{RT\rho_M w_g}\right)^{-1}, \quad (1)$$

172 where M is the average molar mass of the gas phase, R is the universal gas constant (8.3144
 173 J/mol K) and ρ_M is the volatile-free magma density (Burgisser et al., 2015). Magma den-
 174 sity (ρ_m) is a function of the density and volume fraction of both melt and gas (Spera,
 175 2000):

$$176 \quad \rho_m = \rho_g V_g + \rho_M (1 - V_g). \quad (2)$$

177 V_g increases during magma decompression and hence decreases ρ_m . Since ρ_m changes
 178 with p , magma compressibility (β_m) can be linked to the density and density gradient
 179 of magma with respect to pressure (Huppert & Woods, 2002):

$$180 \quad \beta_m = \frac{1}{\rho_m} \frac{\delta \rho_m}{\delta p}. \quad (3)$$

181 Given how ρ_m changes with V_g , magma compressibility is dominated by the weight frac-
 182 tion of exsolved gas phase and hence magmatic volatile content (Kilbride et al., 2016;
 183 Edmonds et al., 2018).

184 Permeability develops when gas bubbles coalesce to form porous networks, thereby
 185 allowing exsolved volatiles to percolate through magma efficiently (Lowenstern, 1994; Can-
 186 dela, 1997; Bachmann & Bergantz, 2006; Collins et al., 2009; Lindoo et al., 2017). Magma
 187 becomes permeable when it reaches critical porosity, which is also defined as the perco-
 188 lation threshold (ϕ_c). In this study, we use gas volume fraction (V_g) to represent magma
 189 porosity and assume that magma becomes permeable and degasses as it reaches the per-
 190 colation threshold. The value of ϕ_c is widely variable, ranging from ~ 17 -78 vol%, due
 191 to the complex interplay between magma properties and physical processes such as melt
 192 viscosity and decompression rate (Rust & Cashman, 2011; Burgisser et al., 2017; Colom-
 193 bier et al., 2020). For melts with low viscosity and overpressure, such as the basaltic melts
 194 considered here, bubbles can grow and rise buoyantly, which reduces the likelihood of
 195 the bubbles coalescing to form a porous network. Colombier et al. (2020) suggest that
 196 low viscosity melts would become permeable at $\phi_c > 37$ vol% and we use that thresh-
 197 old here.

198 **3.2 Linking magma properties to observable parameters**

199 **3.2.1 Deformation**

200 Satellite-based observations of subsurface volume change (derived from inverting
 201 measurements of surface deformation) may be compared to the model of magma prop-
 202 erties during degassing. We define the normalised volume change, \bar{V} , as the ratio between
 203 the subsurface volume change (ΔV_c) and the volume erupted (V_e ; assuming dense-rock
 204 equivalent, DRE):

$$205 \quad \bar{V} = \frac{\Delta V_c}{V_e} = \left(1 + \frac{\beta_m}{\beta_c}\right)^{-1}, \quad (4)$$

206 where β_m is magma compressibility and β_c is chamber compressibility (Rivalta & Segall,
 207 2008; Kilbride et al., 2016). Note that the definition of \bar{V} is the inverse of that from Kilbride
 208 et al. (2016), i.e., $r = \bar{V}^{-1}$. In an elastic half-space, chamber compressibility is affected
 209 by host rock properties and chamber geometry, which can be defined as

$$210 \quad \text{Spherical point source:} \quad \beta_c = \frac{3}{4\mu} \quad (5)$$

$$211 \quad \text{Prolate chamber:} \quad \beta_c = \frac{1}{\mu} \quad (6)$$

$$212 \quad \text{Horizontal oblate ellipsoid (sill):} \quad \beta_c = \frac{1}{\mu} \left(\frac{a}{c} \frac{3}{2\pi} - \frac{3}{5} \right) \quad (7)$$

213 where μ is the shear modulus of the crust and $\frac{a}{c}$ is the ratio of major to minor semi-axes
 214 of an oblate ellipsoid (Amoruso & Crescentini, 2009; Anderson & Segall, 2011).

215 For compressible magmas, ΔV_c would be less than V_e (i.e., $\bar{V} < 1$), such that com-
 216 pressible magmas with low β_c/β_m have low volume change per unit erupted (Voight et
 217 al., 2010), while ΔV_c would be approximately equal to V_e (i.e., $\bar{V} \approx 1$) for incompress-
 218 ible magmas and high β_c/β_m . Since chamber geometry and host rock properties also af-
 219 fect β_c and hence the magnitude of \bar{V} , volcanoes with compressible magmas and rigid
 220 surrounding crust (i.e., high μ and low β_c) cause small volume changes during an erup-
 221 tion (Rivalta & Segall, 2008; Kilbride et al., 2016).

222 A directly observable parameter is surface deformation. Here we define normalised
 223 displacement \bar{z} as the maximum vertical displacement per unit volume erupted. For sim-
 224 plicity, we only calculate the normalised displacement for a spherical point source in a
 225 uniform and elastic half-space (Mogi, 1958), $\bar{z} = \bar{V} \frac{1-v}{\pi} \frac{1}{d^2}$, where v is Poisson's ratio
 226 and d is the depth of magma chamber, although other models are also available (Okada,

227 1985; Yang et al., 1988; Fialko et al., 2001; Masterlark, 2003; Albino et al., 2019; Zhan
228 et al., 2019). \bar{z} is vertically above the source of deformation.

229 **3.2.2 Degassing**

230 Observations of SO₂ degassing are made by satellite-based sensors (e.g., Prata &
231 Kerkmann, 2007; Carn et al., 2016; Theys et al., 2019). We define normalised SO₂ (\bar{S})
232 as the observed SO₂ emitted (E^{SO_2}), normalised by the volume of magma erupted (V_e).
233 \bar{S} estimates the mass of SO₂ per unit volume of magma:

$$234 \quad \bar{S} = \frac{E^{\text{SO}_2}}{V_e} = \frac{m^{\text{SO}_2} M^{\text{SO}_2} \rho_e w_g}{M_g}, \quad (8)$$

235 where m^{SO_2} is the mole fraction of SO₂ in gaseous phase, M^{SO_2} is the molecular mass
236 of SO₂, $\rho_e = 2800 \text{ kg m}^{-3}$ is the erupted rock density, and M_g is the mean molecular mass
237 of the gas phase. For explosive eruptions, we assume that the mass of SO₂ emissions at
238 the surface (E^{SO_2}) is the same as the mass of SO₂ in equilibrium with magma at cham-
239 ber depth, meaning that there is no additional degassing as magma rises from the cham-
240 ber to the surface (Figure 1b). For effusive eruptions, volatiles exsolve in the conduit as
241 magma ascends slowly such that SO₂ degassing is dominated by co-eruptive degassing
242 (Figure 1c). For simplicity, we assume all exsolved SO₂ is emitted as SO₂ in the plume
243 (i.e., there are no other sulfur-bearing species present) and that all SO₂ can be detected
244 by satellites. We ignore sulfur loss due to leaching, sulfur scrubbing by hydrothermal sys-
245 tems, and the formation of sulfide globules during sulfide saturation.

246 **4 One-at-a-time Sensitivity Tests**

247 In this section, we explore the sensitivity of the calculated magma properties to ini-
248 tial magmatic H₂O content ($w^{\text{H}_2\text{O}}$), magmatic CO₂ content (w^{CO_2}), oxygen fugacity (f_{O_2}),
249 magmatic S content (w^{S}), crustal shear modulus (μ) and chamber geometry. We con-
250 duct one-at-a-time sensitivity tests by holding other parameters constant and varying
251 the chosen parameter. For each example, we first consider the general sensitivity of the
252 model to changing magma properties by looking at the maximum percentage changes
253 over a range of depths, and then provide an illustrative example for a chamber at a depth
254 of 3 km (i.e., pressure of 82 MPa). While this provides a clear understanding of the role

Table 1. Volatile composition of the parameters explored. The sensitivity tests vary the chosen parameter (bracketed) while holding all other parameters constant (unbracketed).

Parameters	H ₂ O (wt%)	CO ₂ (ppm)	f_{O_2}	S (ppm)
Sensitivity test	2.0* (1.0-3.0)	1000 (500 – 1500)	NNO (NNO – 1-NNO + 1)	2000 (1000-3000)

*All sensitivity tests use constant $w^{\text{H}_2\text{O}} = 2.0$ wt%, except for S, which uses $w^{\text{H}_2\text{O}} = 3.0$ wt%.

of each parameter, it does not consider the co-dependence of input variables, which may result in parameter combinations that are not physically realistic.

Bulk magma volatile contents are informed by observations of dissolved volatile content from melt inclusions of basalts. For simplicity, we assume an isothermal magma at 1200 °C. We explore $w^{\text{H}_2\text{O}}$, w^{CO_2} and w^{S} in the ranges of 1.0 to 3.0 wt% H₂O, 500 to 1500 ppm CO₂, and 1000 to 3000 ppm S, respectively (Table 1). We use f_{O_2} from NNO–1 to NNO+1 to explore the effects of oxygen fugacity on the solubility of volatile species. To test how chamber compressibility (β_c) affects volcanic deformation, we use μ from 0.1 to 30 GPa (Heap et al., 2020), and consider three chamber geometries: a spherical point source, a vertical prolate ellipsoid (pipe-like chamber) and a horizontal oblate ellipsoid (sill) (Gudmundsson, 2008; Amoroso & Crescentini, 2009; Anderson & Segall, 2011). Although we do not expect the gas to remain in contact with the magma when V_g exceeds the percolation threshold at which magma becomes permeable, i.e., $\phi_c > 37$ vol% (Colombier et al., 2020), we run our sensitivity tests all the way to the surface. Table 2 summarises the maximum percentage change over the depth range of each parameter on the estimated values of \bar{S} , \bar{V} and \bar{z} .

4.1 Effects of H₂O content on magma properties

First, we vary the initial dissolved H₂O content $w^{\text{H}_2\text{O}}$ in the melt and investigate how it affects magma properties ρ_m and β_m , and observables \bar{S} , \bar{V} and \bar{z} (Figure 2) during ascent and degassing. In this sensitivity test, $w^{\text{H}_2\text{O}}$ ranges from 1.0-3.0 wt% and the constant parameters are $w^{\text{CO}_2} = 1000$ ppm, $f_{\text{O}_2} = \text{NNO}$, $w^{\text{S}} = 2000$ ppm. We assume a fixed chamber compressibility for a spherical cavity $\beta_c = \frac{3}{4\mu}$ where $\mu = 2.1$ GPa (i.e., $\beta_c = 3.6 \times 10^{-10}$ Pa⁻¹).

Solubility decreases with decreasing pressure for each volatile component, so as pressure decreases, the mass fraction dissolved in the melt (w_M^x) decreases and the mole frac-

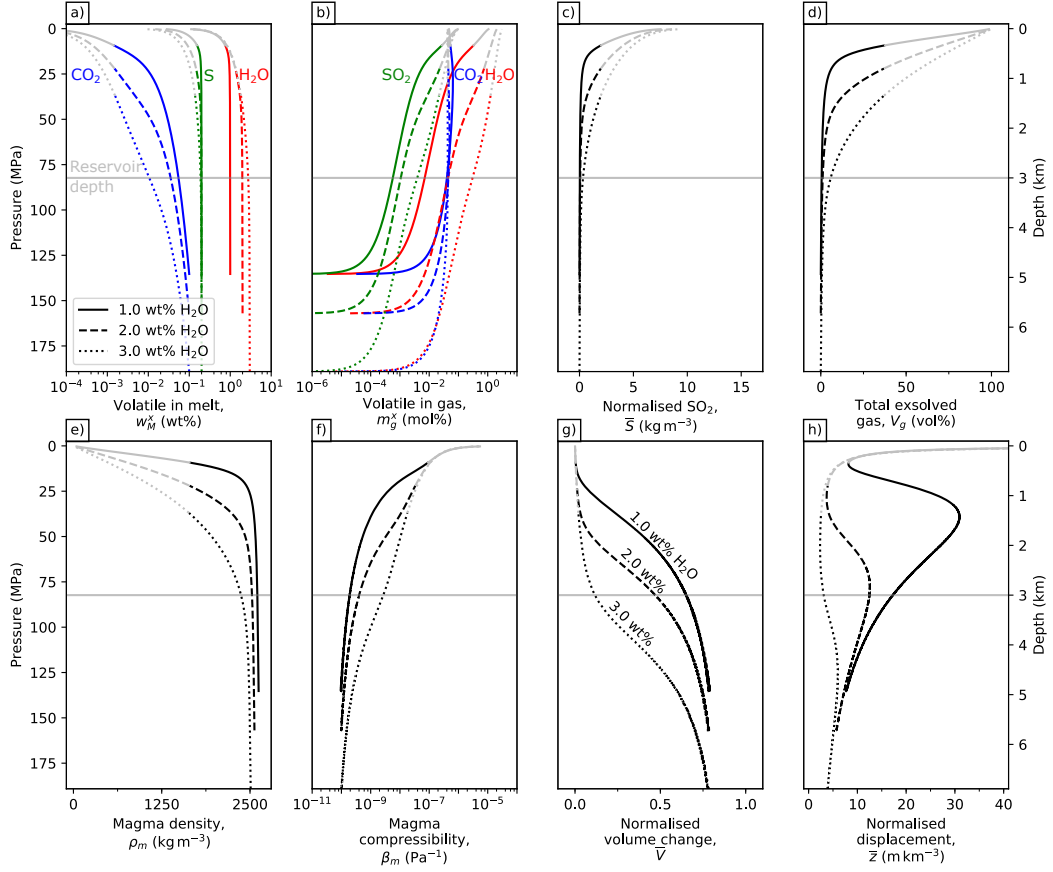


Figure 2. Physicochemical properties of basalts when varying the initial magmatic H₂O from 1.0-3.0 wt%. (a) Weight fraction of dissolved H₂O, CO₂ and S in melt (w_M^x). (b) Mole fraction of exsolved H₂O, CO₂ and SO₂ in gas (m_g^x). (c) Mass of SO₂ gas per unit volume of magma, also defined as normalised SO₂ (\bar{S}). (d) Volume fraction of exsolved gases in magma (V_g). (e) Magma density (ρ_m). (f) Magma compressibility (β_m). (g) Model predicted volume change normalised by unit volume of magma (\bar{V}). (h) Maximum vertical displacement normalised by unit volume of magma (\bar{z}). The grey lines represent magma properties after exceeding percolation threshold $\phi_c = 37$ vol%. Fixed parameters: $w^{\text{CO}_2} = 1000$ ppm, $f_{\text{O}_2} = \text{NNO}$, $w^{\text{S}} = 2000$ ppm and $\mu = 2.1$ GPa.

Table 2. Summary table showing the maximum percentage change of each observation when increasing the values of each parameter (shown in brackets) while holding other parameters constant.

Parameters	Normalised SO ₂ , \bar{S} (kg m ⁻³)	Normalised volume change, \bar{V}	Normalised displacement, \bar{z} (m km ⁻³)
Magmatic H ₂ O, $w^{\text{H}_2\text{O}}$ (1.0-3.0 wt%)	+370%	-83%	-92%
Magmatic CO ₂ , w^{CO_2} (500-1500 ppm)	+74%	-37%	-44%
Oxygen fugacity, f_{O_2} (NNO-1-NNO+1)	+110%	+15%	+17%
Magmatic S, w^{S} (1000-3000 ppm)	+130%	-5.3%	-0.35%
Crustal shear modulus, μ (0.1-30 GPa)	n/a	-94%	-98%

280 tion that has exsolved to the gaseous phase (m_g^x) increases (Figure 2a-b). Higher $w^{\text{H}_2\text{O}}$
 281 reduces the solubility of CO₂ and S (Figure 2a), thus increasing the mole fraction of $m_g^{\text{H}_2\text{O}}$,
 282 $m_g^{\text{CO}_2}$ and m_g^{S} (Figure 2b). Normalised SO₂ (\bar{S}) represents the mass of exsolved SO₂ per
 283 unit volume of magma, assuming that melt and gas do not segregate. By increasing $w^{\text{H}_2\text{O}}$
 284 by a factor of 3, \bar{S} increases up to a maximum of $\sim 370\%$ at 0.51 km depth (Figure 2c).
 285 Gas volume fraction (V_g) increases as volatiles exsolve and gas bubbles expand at lower
 286 pressures. Since V_g is dominated by $w^{\text{H}_2\text{O}}$, V_g increases up to a maximum of $\sim 440\%$ at
 287 0.58 km depth when increasing $w^{\text{H}_2\text{O}}$ from 1.0 to 3.0 wt% (Figure 2d).

288 The increase in $w^{\text{H}_2\text{O}}$ increases V_g , which decreases magma density (ρ_m ; Equation
 289 2; Figure 2e) and increases magma compressibility (β_m ; Equation 3; Figure 2f). There-
 290 fore, with the increase of $w^{\text{H}_2\text{O}}$ from 1-3 wt%, β_m increases up to a maximum of $\sim 1900\%$
 291 at 2.1 km depth (Figure 2f), and normalised volume change (\bar{V}) decreases up to a max-
 292 imum of $\sim 83\%$ at 2.9 km depth (Figure 2g). Based on the simple Mogi model, there
 293 is a trade-off between volume change and depth, such that the same volume change will
 294 cause a larger displacement at a shallow depth. However, when V_g and β_m are consid-
 295 ered, the maximum vertical displacement per unit volume (\bar{z}) does not vary in a sim-
 296 ple way; the increase in V_g towards the surface causes a local minimum in \bar{z} at 0.5 km
 297 depth. Given that \bar{z} is controlled by chamber depth and \bar{V} , increasing $w^{\text{H}_2\text{O}}$ thus causes
 298 a relative decrease in the normalised displacement (\bar{z}) up to a maximum of $\sim 92\%$ at
 299 1.4 km depth (Figure 2h).

300 To illustrate these results, we give specific values for a chamber depth of 3 km. Vary-
 301 ing $w^{\text{H}_2\text{O}}$ from 1.0 to 3.0 wt% increases \bar{S} from 0.025 kg m^{-3} to 0.32 kg m^{-3} (Figure 2c).
 302 V_g increases from 0.47 vol% to 5.8 vol%, which corresponds to the increase in β_m from
 303 $1.9 \times 10^{-10} \text{ Pa}^{-1}$ to $27 \times 10^{-10} \text{ Pa}^{-1}$ (Figure 2f). As a result, \bar{V} decreases from 0.65 to
 304 0.11 (Figure 2g) and \bar{z} is reduced from 17 m km^{-3} to 3.1 m km^{-3} (Figure 2h). The model
 305 thus predicts that basalts with higher initial H_2O content have greater \bar{S} and β_m , and
 306 as a result, lower \bar{V} and \bar{z} (Figure 2).

307 4.2 Effects of CO_2 content on magma properties

308 Here, we vary initial dissolved CO_2 content to understand how it affects magma
 309 properties and observables \bar{S} , \bar{V} and \bar{z} (Figure 3). We use w^{CO_2} in the range of 500 ppm
 310 to 1500 ppm and fixed $w^{\text{H}_2\text{O}} = 2.0 \text{ wt}\%$, $f_{\text{O}_2} = \text{NNO}$, $w^{\text{S}} = 2000 \text{ ppm}$ and $\mu = 2.1 \text{ GPa}$
 311 for this model.

312 Figure 3a shows that increasing w^{CO_2} from 500 ppm to 1500 ppm increases the amount
 313 of dissolved $w_M^{\text{CO}_2}$ up to a maximum of 55% at 1.5 km depth, but decreases $w_M^{\text{H}_2\text{O}}$ and
 314 w_M^{S} by $<5.3\%$ and $<4.1\%$, respectively. This results in a relative increase in the amount
 315 of exsolved SO_2 ($m_g^{\text{SO}_2}$) and \bar{S} up to a maximum of $\sim 80\%$ and $\sim 74\%$, respectively, at
 316 1.5 km depth (Figure 3b-c). Similarly, varying initial CO_2 content increases V_g up to a
 317 maximum of $\sim 72\%$ at 1.5 km depth (Figure 3d). Increasing w^{CO_2} corresponds to an in-
 318 crease in β_m up to a maximum of $<54\%$ and a decrease in \bar{V} up to a maximum of 37%
 319 at 2.9 km depth (Figure 3f-g), which correlates to the decrease in \bar{z} up to a maximum
 320 of 44% at 2.5 km depth (Figure 3h).

321 Here, we quantify these results for a depth of 3 km to illustrate the sensitivity to
 322 w^{CO_2} . Increasing initial CO_2 from 500 ppm to 1500 ppm increases \bar{S} from 0.014 kg m^{-3}
 323 to 0.10 kg m^{-3} and V_g from 0.26 vol% to 1.9 vol% (Figure 3c-d). This corresponds to
 324 an increase in β_m from $2.3 \times 10^{-10} \text{ Pa}^{-1}$ to $5.6 \times 10^{-10} \text{ Pa}^{-1}$ (Figure 3f). As a result, \bar{V}
 325 decreases from 0.61 to 0.39 (Figure 3g). and \bar{z} is reduced from 16 m km^{-3} to 10 m km^{-3}
 326 (Figure 3h). The model shows that increasing initial CO_2 content from 500 ppm to 1500
 327 ppm causes significant changes to both \bar{V} and \bar{z} , but they are approximately half that
 328 of varying $w^{\text{H}_2\text{O}}$ from 1.0 wt% to 3.0 wt%. As such, variations in H_2O content have a
 329 greater effect on co-eruptive deformation than variations in CO_2 content.

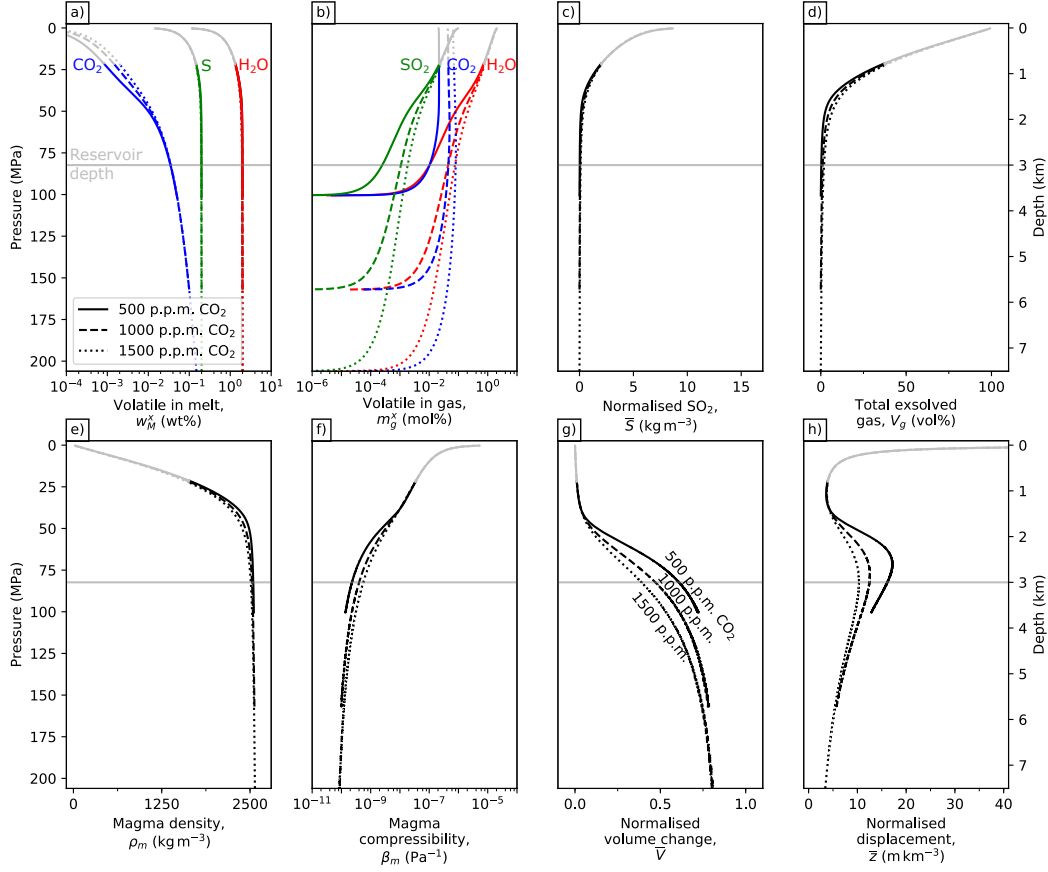


Figure 3. Physicochemical properties of basalts when varying the initial weight fraction of dissolved CO_2 (w^{CO_2}) from 500 to 1500 ppm. (a) Weight fraction of dissolved H_2O , CO_2 and S in melt (w_M^x). (b) Mole fraction of exsolved H_2O , CO_2 and SO_2 in gas (m_g^x). (c) Mass of SO_2 gas per unit volume of magma, also defined as normalised SO_2 (\bar{S}). (d) Volume fraction of exsolved gases in magma (V_g). (e) Magma density (ρ_m). (f) Magma compressibility (β_m). (g) Model predicted volume change normalised by unit volume of magma (\bar{V}). (h) Maximum vertical displacement normalised by unit volume of magma (\bar{z}). The grey lines represent magma properties after exceeding percolation threshold $\phi_c = 37$ vol%. Fixed parameters: $w^{\text{H}_2\text{O}} = 2.0$ wt%, $f_{\text{O}_2} = \text{NNO}$, $w^{\text{S}} = 2000$ ppm and $\mu = 2.1$ GPa.

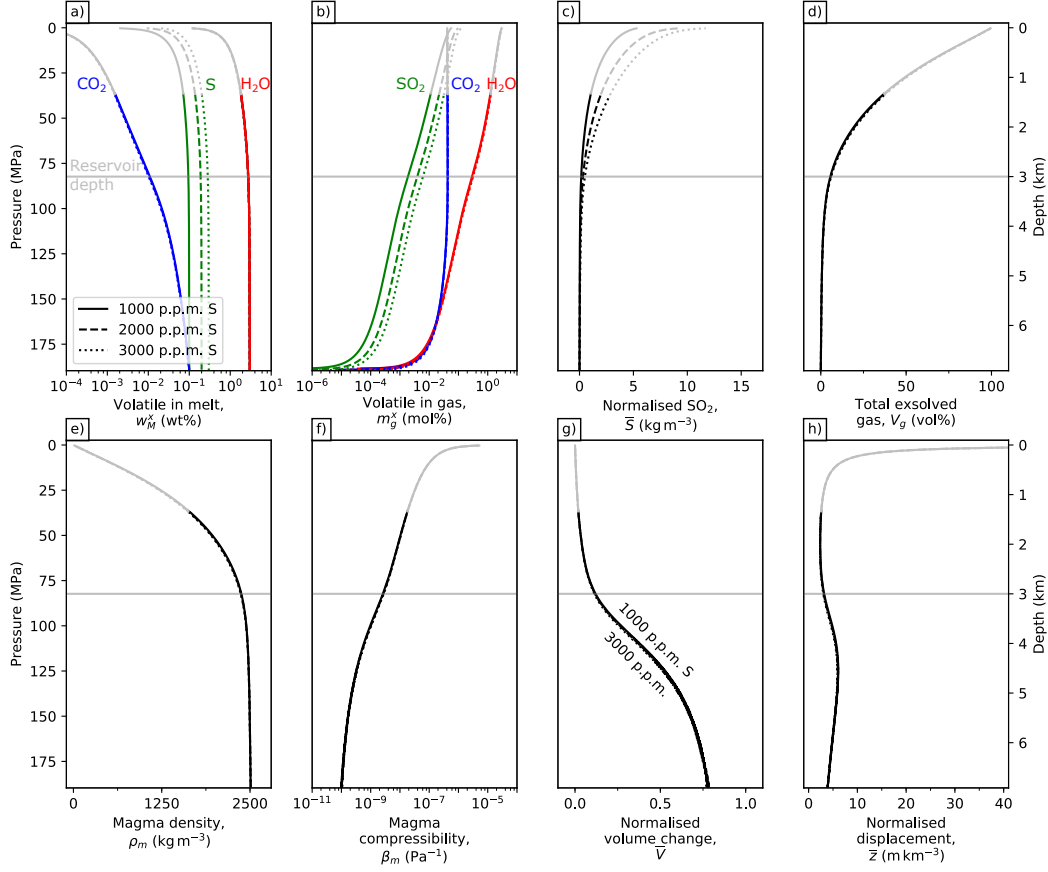


Figure 4. Physicochemical properties of basalts when varying the initial weight fraction of dissolved S (w^S) from 1000 to 3000 ppm. (a) Weight fraction of dissolved H_2O , CO_2 and S in melt (w_M^x). (b) Mole fraction of exsolved H_2O , CO_2 and SO_2 in gas (m_g^x). (c) Mass of SO_2 gas per unit volume of magma, also defined as normalised SO_2 (\bar{S}). (d) Volume fraction of exsolved gases in magma (V_g). (e) Magma density (ρ_m). (f) Magma compressibility (β_m). (g) Model predicted volume change normalised by unit volume of magma (\bar{V}). (h) Maximum vertical displacement normalised by unit volume of magma (\bar{z}). The grey lines represent magma properties after exceeding percolation threshold $\phi_c = 37$ vol%. Fixed parameters: $w^{\text{H}_2\text{O}} = 3.0$ wt%, $w^{\text{CO}_2} = 1000$ ppm, $f_{\text{O}_2} = \text{NNO}$ and $\mu = 2.1$ GPa.

330

4.3 Effects of sulfur content

331

332

333

334

Here, we vary initial dissolved sulfur (S) content to understand how it affects magma properties and observables \bar{S} , \bar{V} and \bar{z} (Figure 4). We use w^S in the range of 1000 ppm to 3000 ppm and fixed $w^{\text{H}_2\text{O}} = 3.0$ wt%, $w^{\text{CO}_2} = 1000$ ppm, $f_{\text{O}_2} = \text{NNO}$ and $\mu = 2.1$ GPa for this model.

335

336

337

338

339

340

341

Figure 4a shows that w_M^S increases by $<200\%$ at 6.9 km depth with increasing w^S from 1000 ppm to 3000 ppm, which corresponds to the increase in $m_g^{\text{SO}_2}$ and \bar{S} up to a maximum of $\sim 138\%$ and $\sim 130\%$ at the surface, respectively (Figure 4b-c). The total gas volume fraction, however, increases by only $<3\%$ at 1.4 km depth (Figure 4d). Since varying initial S content has minimal impact on V_g , β_m only increases by $<9.3\%$ at 3.6 km depth (Figure 4f), which correlates to the decrease in \bar{V} by less than 5.3% at 3.9 km depth and \bar{z} less than 0.35% at the surface (Figure 4g-h).

342

343

344

345

346

347

348

349

350

We quantify these results for a depth of 3 km to illustrate the effect of varying w^S from 1000 ppm to 3000 ppm. This range of sulfur is less than the sulfur content at sulfide saturation. Increasing magmatic w^S increases \bar{S} from 0.15 kg m^{-3} to 0.50 kg m^{-3} (Figure 4c), which can be linked to the increase in V_g from 5.6 vol% to 6.0 vol% (Figure 4d). This corresponds to a very small increase in β_m from $2.6 \times 10^{-9} \text{ Pa}^{-1}$ to $2.8 \times 10^{-9} \text{ Pa}^{-1}$ (Figure 4f). The increase in β_m thus reduces both \bar{V} and \bar{z} marginally from 0.12 to 0.11 and 3.2 m km^{-3} to 3.0 m km^{-3} , respectively (Figure 4g-h). The model shows that basalts with high initial w^S release high \bar{S} but β_m and hence co-eruptive deformation is only minimally affected.

351

4.4 Effects of oxygen fugacity on magma properties

352

353

354

355

356

357

358

359

Figure 5 shows how varying oxygen fugacity (f_{O_2}) affects magma properties, and consequently observables \bar{S} , \bar{V} and \bar{z} . We vary f_{O_2} from NNO-1 to NNO+1 and fix $w^{\text{H}_2\text{O}} = 2.0$ wt%, $w^{\text{CO}_2} = 1000$ ppm, $w^S = 2000$ ppm and $\mu = 2.1$ GPa for this model.

The model predicts that varying f_{O_2} from NNO-1 to NNO+1 increases $w_M^{\text{CO}_2}$, $w_M^{\text{H}_2\text{O}}$ and w_M^S up to a maximum of 2.3%, 9.0% and 32% at depths of 2.9, 7.1 and 2.1 km, respectively, due to the effect of oxygen fugacity on the solubility of each volatile species (Figure 5a). The significant increase in w_M^S causes a relative increase $m_g^{\text{SO}_2}$ and \bar{S} up to a maximum of 119% and 112%, respectively, at 0.4 km depth (Figure 5b-c).

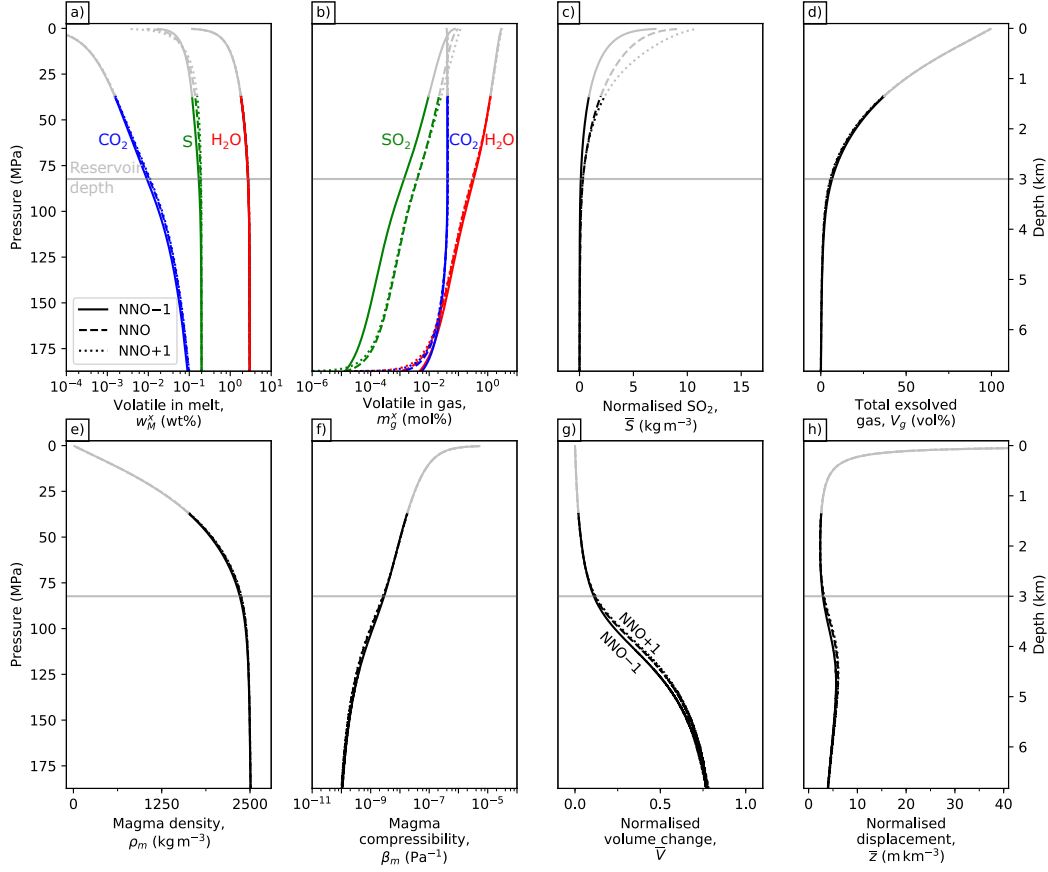


Figure 5. Physicochemical properties of basalts when varying f_{O_2} of magma storage from NNO-1 to NNO+1. (a) Weight fraction of dissolved H_2O , CO_2 and S in melt (w_M^x). (b) Mole fraction of exsolved H_2O , CO_2 and SO_2 in gas (m_g^x). (c) Mass of SO_2 gas per unit volume of magma, also defined as normalised SO_2 (\bar{S}). (d) Volume fraction of exsolved gases in magma (V_g). (e) Magma density (ρ_m). (f) Magma compressibility (β_m). (g) Model predicted volume change normalised by unit volume of magma (\bar{V}). (h) Maximum vertical displacement normalised by unit volume of magma (\bar{z}). The grey lines represent magma properties after exceeding percolation threshold $\phi_c = 37$ vol%. Fixed parameters: $w^{\text{H}_2\text{O}} = 2.0$ wt%, $w^{\text{CO}_2} = 1000$ ppm, $w^{\text{S}} = 2000$ ppm and $\mu = 2.1$ GPa.

360 However, V_g is reduced by only <11% at 2.8 km depth so varying f_{O_2} has mini-
 361 mal impact on ρ_m and β_m (Figure 5e). In fact, increasing f_{O_2} from NNO-1 to NNO+1
 362 decreases β_m by 20% at 4.2 km depth (Figure 5f) and hence \bar{V} of oxidised basalts is <15%
 363 greater than its reduced counterpart at 4.2 km depth (Figure 5g). While \bar{z} is controlled
 364 by chamber depth and \bar{V} , the maximum increase in \bar{z} of less than 17% also occur at 4.2
 365 km depth due to insignificant difference in \bar{V} when varying f_{O_2} (Figure 5h).

366 Next, we quantify the predictions for a depth of 3 km. Varying f_{O_2} from NNO-1
 367 to NNO+1 increases \bar{S} from 0.11 kg m^{-3} to 0.31 kg m^{-3} (Figure 5c). However, V_g de-
 368 creases from 6.6 vol% to 5.5 vol%, which corresponds to a decrease in β_m from 2.9×10^{-10}
 369 Pa^{-1} to $2.6 \times 10^{-10} \text{ Pa}^{-1}$ (Figure 5f). As a result, \bar{V} and \bar{z} increases from 0.11 to 0.12
 370 and 2.9 m km^{-3} to 3.2 m km^{-3} , respectively (Figure 5g-h). The model thus predicts that
 371 while oxidised basalts have greater \bar{S} than reduced basalts, variations in oxygen fugac-
 372 ity of basalts has minimal impact on co-eruptive deformation.

373 4.5 Effects of chamber compressibility

374 Crustal properties and chamber geometry are known to have a major role in de-
 375 termining surface deformation (e.g., Gudmundsson, 2008; Amoruso & Crescentini, 2009;
 376 Anderson & Segall, 2011; Heap et al., 2020). Here we investigate the two parameters that
 377 directly affect our simplified model using the same sensitivity analysis as for the other
 378 parameters. \bar{V} is a function of β_m and β_c , and the two parameters we explore in this sec-
 379 tion are crustal shear modulus and chamber geometry that control β_c and thus affect \bar{V}
 380 (Equation 4). We use a range of crustal shear modulus (μ) from 0.1 GPa (compliant crust)
 381 to 30 GPa (non-compliant crust), which is typical in volcanic areas (Gudmundsson, 2005;
 382 Rivalta & Segall, 2008). It is noted that μ changes with depth but for simplicity, we as-
 383 sume a constant μ at all depths considering the variations in and between volcanic re-
 384 gions are likely to be larger than those with depth. We considered three representative
 385 chamber geometries, which are a spherical point source, a vertical prolate ellipsoid (pipe-
 386 like chamber) and a horizontal oblate ellipsoid (sill), and use $\frac{a}{c} = 100$ for the horizon-
 387 tal sill (Equation 5) (Amoruso & Crescentini, 2009; Anderson & Segall, 2011). We use
 388 a Poisson's ratio ν of 0.30 based on the average value for volcanic rock with average poros-
 389 ity and fracture density (Heap et al., 2020). The sensitivity test uses fixed parameters
 390 of $w^{\text{H}_2\text{O}} = 2.0 \text{ wt}\%$, $w^{\text{CO}_2} = 700 \text{ ppm}$, $f_{\text{O}_2} = \text{NNO}$, and $w_g = 0.01 \text{ wt}\%$.

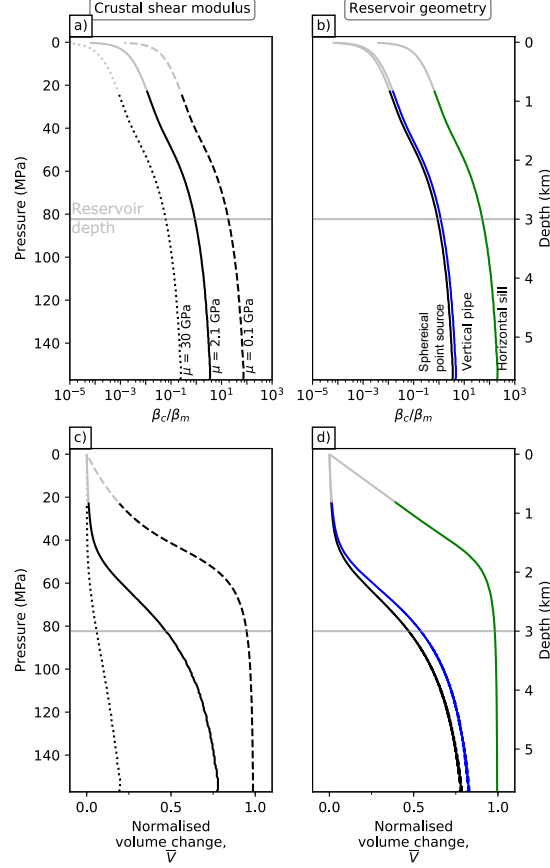


Figure 6. Physical properties of basalts when varying the crustal shear modulus (μ) from 0.1 to 30 GPa and chamber geometry. (a) The ratio of β_c/β_m to illustrate the effects of crustal shear modulus and chamber geometry. The μ used are 0.1 GPa, 2.1 GPa and 30 GPa (Heap et al., 2020), and the chamber geometries considered are a spherical point source, a vertical pipe-like chamber and a horizontal sill (Amoruso & Crescentini, 2009). Different μ and chamber geometries are represented by different line styles and colour, respectively. (b) Model predicted normalised volume change (\bar{V}) for a spherical point source, a vertical pipe-like chamber and a horizontal sill with $\mu = 2.1$ GPa. The major to minor semiaxis of the horizontal sill, $\frac{a}{c}$, is 100. (c) \bar{V} for a spherical point source with varying μ . (d) \bar{V} for a spherical point source, a vertical pipe-like chamber and a horizontal sill with $\mu = 2.1$ GPa. Fixed parameters: $w^{\text{H}_2\text{O}} = 2.0$ wt%, $w^{\text{CO}_2} = 1000$ ppm, $f_{\text{O}_2} = \text{NNO}$, and $w^{\text{S}} = 2000$ ppm. The grey lines represent magma properties when percolation threshold exceeds $\phi_c = 37$ vol%.

391 To understand how crustal properties affect volcanic deformation, we first discuss
 392 the effects of μ and chamber geometry on the ratio of β_c/β_m . Since β_c is inversely pro-
 393 portional to μ , a crust with $\mu = 0.1$ GPa results in $\beta_c/\beta_m = 19$ for a chamber at 3 km
 394 depth, while $\beta_c/\beta_m = 0.062$ for a crust with $\mu = 30$ GPa (Figure 6a). From Equation 5,
 395 we find that the crustal compressibility β_c for chambers with a vertical pipe-like shape
 396 is 33% higher than a spherical point source (Figure 6b). An ellipsoid with $\frac{a}{c} = 100$ has
 397 the highest β_c among the three chamber geometries (i.e., 60 times greater than a spher-
 398 ical point source), consistent with analytical results from Anderson and Segall (2011).

399 Here we quantify the effects of varying μ and the chamber geometry on \bar{V} (Figure
 400 6c-d). The \bar{V} for crustal rocks with $\mu = 0.1$ GPa is up to a maximum of $\sim 360\%$ greater
 401 than that with $\mu = 2.1$ GPa at 2.1 km depth. In contrast, \bar{V} is reduced up to a max-
 402 imum of $\sim 74\%$ at 5.7 km depth for a crust with $\mu = 30$ GPa when compared to $\mu =$
 403 2.1 GPa. At 3 km depth, the \bar{V} for $\mu = 0.1$ GPa, 2.1 GPa and 30 GPa are 0.95, 0.47 and
 404 0.058, respectively (Figure 6c). The effects of different chamber geometries on \bar{V} are shown
 405 in Figure 6d, with $\mu = 2.1$ GPa and Poisson's ratio ν of 0.30 (Heap et al., 2020). The
 406 normalised volume change \bar{V} is greatest for horizontal sills and smallest for spherical point
 407 source, such that $\bar{V} = 0.98$ and 0.47, respectively, for a chamber at 3 km depth. Based
 408 on the effects of μ and chamber geometry on β_c/β_m , we find that a volcano with low β_c/β_m
 409 (i.e., spherical, high shear modulus) has low \bar{V} which indicates muted volcanic deforma-
 410 tion. In contrast, a volcano with high β_c/β_m (i.e., horizontal sill, low shear modulus) has
 411 high \bar{V} . For example, at 3 km depth, $\bar{V} = 0.058$ for a spherical point source with $\mu =$
 412 30 GPa, but $\bar{V} = 1.0$ for a sill with $\mu = 0.1$ GPa.

413 The main takeaways from the sensitivity analysis of chamber compressibility is that
 414 1) spherical point sources and vertical pipe-like chambers have similar β_c/β_m and \bar{V} , whereas
 415 sills have higher β_c/β_m and thus high \bar{V} (Figure 6b,d) and 2) crustal properties, specif-
 416 ically shear modulus, have a significant influence on \bar{V} , with lower crustal shear mod-
 417 ulus causing larger volume changes (Figure 6a,c) (Heap et al., 2020; Hautmann et al.,
 418 2010).

419 4.6 Summary of sensitivity analyses

420 Here we summarise the results from each sensitivity test. A summary of the max-
 421 imum percentage change of \bar{S} , \bar{V} and \bar{z} over the depth range of each parameter are shown
 422 in Table 2. We find that eruptions of water-rich magmas have higher SO₂ emissions and

423 less deformation for a particular volume of magma erupted. While initial magmatic CO₂
 424 causes insignificant changes to the total amount of SO₂ degassing during eruptions, it
 425 has a moderate influence on the observed co-eruptive deformation, i.e., CO₂-rich mag-
 426 mas are more compressible. Initial magmatic S and oxygen fugacity have a strong in-
 427 fluence on the magnitude of SO₂ degassing but have a minimal impact on the magni-
 428 tude of the co-eruptive deformation. Magmas with a high oxygen fugacity yield high SO₂
 429 emissions during an eruption, but this does not impact co-eruptive deformation signif-
 430 icantly. Magmatic reservoirs with strong surrounding crustal rocks (i.e., high μ) and spher-
 431 ical geometry may display muted co-eruptive deformation.

432 **5 Comparison Between Arc Basalts and Ocean Island Basalts**

433 **5.1 Thermodynamic modelling of magma properties**

434 We now examine how tectonic setting influences the physicochemical properties of
 435 basaltic magma and consequently its impact on observed volcanic deformation and SO₂
 436 degassing. Here we compare arc basalts and ocean island basalts by considering realis-
 437 tic parameter combinations and the co-dependence of parameters. Basaltic magma in
 438 arc settings tends to have higher water contents than basaltic magma from ocean island
 439 settings (e.g., Wallace, 2005; Zimmer et al., 2010; Plank et al., 2013). Melt inclusions
 440 data suggest that, on average, arc basalts contain 3.3 wt% H₂O, 1000 ppm CO₂ and 1200
 441 ppm S, and ocean island basalts contain 1.0 wt% H₂O, 500 ppm CO₂ and 1100 ppm S
 442 (Wallace, 2005; Plank et al., 2013). These values represent the dissolved volatile abun-
 443 dances at shallow crustal levels, in which the volatiles recorded in the melt inclusions are
 444 primarily controlled by solubility. We note that arc basalts have been inferred to con-
 445 tain a minimum of 3000 ppm CO₂ from modelling of magma flux and melt inclusions
 446 (Wallace, 2005), but because primitive volatile contents are less well constrained, we se-
 447 lected the values from melt inclusions for simplicity. We take typical values of f_{O_2} of arc
 448 basalts and ocean island basalts from NNO-1 to NNO+1 and NNO-1.4 to NNO-0.4,
 449 respectively, based on examples from the Mexican Volcanic Belt and Kīlauea volcano (e.g.,
 450 Carmichael & Ghiorso, 1986; Wallace & Carmichael, 1999). Crustal compressibility also
 451 influences the magnitude of volcanic deformation (Section 4.5), and thus we use $\mu = 2.1$
 452 GPa, which is typical in volcanic areas, and assume a Mogi deformation source for sim-
 453 plicity (Mogi, 1958; Gudmundsson, 2005; Heap et al., 2020). The range of parameter val-
 454 ues used for the analyses described below are listed in Table 3.

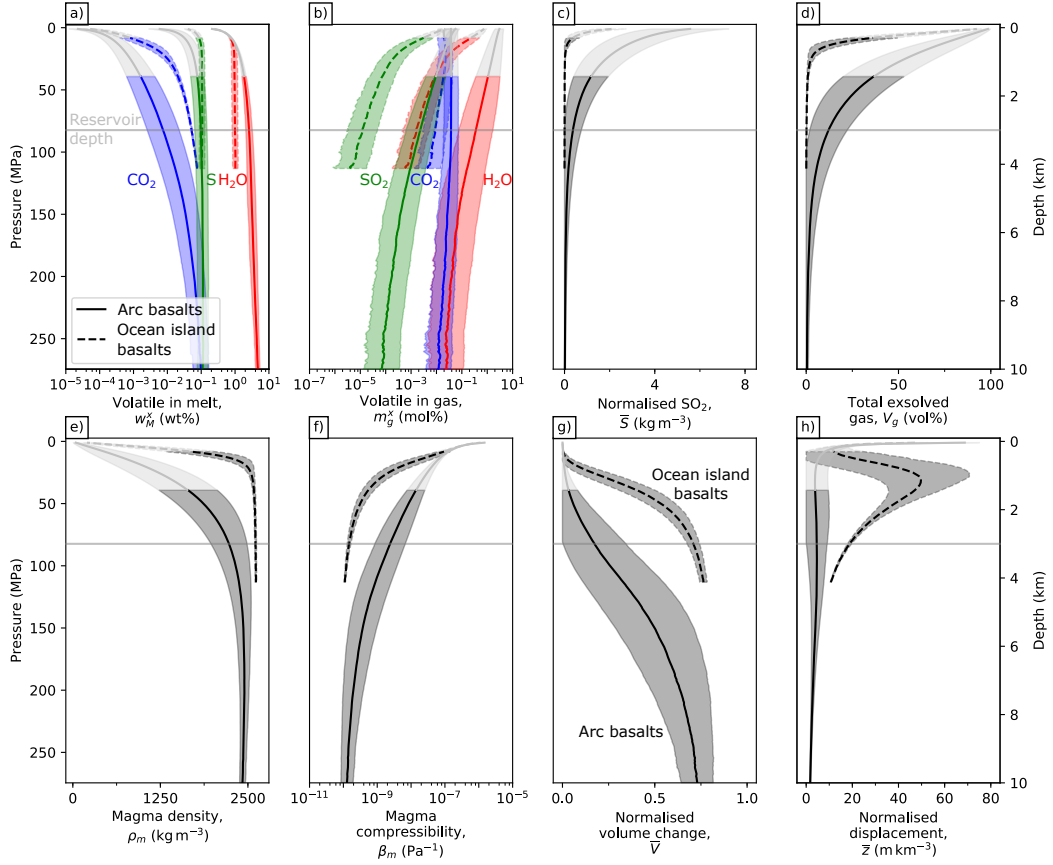


Figure 7. Comparison of magma properties between arc basalts (full line) and ocean island basalts (dashed line). The input parameters for the thermodynamic model ($w^{\text{H}_2\text{O}}$, w^{CO_2} , w^{S} and f_{O_2}) and crustal shear modulus μ are initialised using a Monte-Carlo approach (Table 3). 1000 simulations are performed and the magma properties are calculated using the thermodynamic framework. (a) Weight fraction of dissolved volatile contents and (b) mol fraction of exsolved volatile contents. (c) Normalised SO_2 , \bar{S} . (d) Volume fraction of exsolved gases in magma (V_g). (e) Magma density (ρ_m) and (f) Magma compressibility (β_m). (g) Normalised volume change (\bar{V}). (h) Normalised vertical displacement (\bar{z}). The grey lines represent magma properties after exceeding percolation threshold $\phi_c = 37$ vol% and the shaded region represent 1σ uncertainty. Range of parameter values for arc basalts and ocean island basalts are listed in Table 3.

Table 3. Range of parameters used for Monte-Carlo simulation.

Magma	H ₂ O (wt%)	CO ₂ (ppm)	S (ppm)	f_{O_2}
Arc basalts	3.3 ± 1.0	1000 ± 400	1200 ± 400	NNO ± 0.5
Ocean island basalts	1.0 ± 0.2	500 ± 200	1100 ± 200	NNO $- 1.1 \pm 0.3$

455 Monte-Carlo simulation allows repeated random sampling to estimate possible ranges
456 of magma properties and observations of volcanic eruptions, and as such we use the magma
457 composition of arc basalts and ocean island basalts to estimate the realistic range of magma
458 properties. We performed 1000 simulations for each type using the distribution of each
459 variable (w^{H_2O} , w^{CO_2} , w^S , f_{O_2}) provided in Table 3 as input parameters for the ther-
460 modynamic model. Parameters that are distributed below the detection limit are read-
461 justed accordingly (i.e., $w^{H_2O} < 0$ wt%, $w^{CO_2} < 25$ ppm and $w^S < 50$ ppm are changed
462 to $w^{H_2O} = 1.0$ wt%, $w^{CO_2} = 25$ ppm and $w^S = 50$ ppm, respectively. The thermody-
463 namic model has a starting temperature of 1200 °C, a Poisson’s ratio ν of 0.30, and we
464 find the starting pressure/depth using the saturation point of each melt composition. Af-
465 ter 1000 Monte-Carlo simulations, we calculate the mean and the standard deviation for
466 each model output, such as normalised SO₂, magma compressibility and normalised vol-
467 ume change. Since we started each simulation at the saturation point for that compo-
468 sition (see Section 3.1), we apply a filter to discard the values for any pressure/depth with
469 less than 100 simulations.

470 In Figure 7 we present the model predictions for arc basalts and ocean island basalts
471 to illustrate the effects of tectonic settings on magma properties and co-eruptive obser-
472 vations. Arc basalts have a saturation point of ≈ 10 km, which is higher than that of ocean
473 island basalts at ≈ 4 km depth due to the fact that arc basalts have a higher magmatic
474 volatile content than ocean island basalts. The high f_{O_2} environment of arc basalts will
475 tend to produce more exsolved SO₂ at the expense of H₂S and S₂, whereas ocean island
476 basalts, which have a lower f_{O_2} , have less exsolved SO₂ in the gas phase (Figure 7b). With
477 a higher mole fraction of exsolved SO₂, the predicted \bar{S} of arc basalts is higher than that
478 of ocean island basalts (Figure 7c). The higher magmatic volatile content of arc basalts
479 translates to a higher V_g (Figure 7d), suggesting that in general, arc basalts are more
480 compressible than ocean island basalts (Figure 7f). The increased magma compressibil-
481 ity indicates that arc basalts have a lower \bar{V} and \bar{z} than ocean island basalts (Figure 7g-
482 h).

483 Here we give specific values for arc basalts and ocean island basalts assuming a magma
 484 chamber at 3 km depth (Figure 7). If an explosive eruption (no co-eruptive degassing)
 485 should occur from a chamber at 3 km depth, the predicted \bar{S} of arc basalts is 0.37 kg m^{-3} ,
 486 greater than that of ocean island basalts at 0.0011 kg m^{-3} (Figure 7c). For a chamber
 487 at 3 km depth, arc basalts are more compressible than ocean island basalts at $\beta_m = 2.2 \times 10^{-9}$
 488 Pa^{-1} and $1.2 \times 10^{-10} \text{ Pa}^{-1}$, respectively (Figure 7f), and thus arc basalts have $\bar{V} = 0.17$
 489 and $\bar{z} = 4.6 \text{ m km}^{-3}$ as compared to ocean island basalts that have $\bar{V} = 0.71$ and $\bar{z} =$
 490 19 m km^{-3} . It is noted that ocean island basalts eruptions are usually effusive in nature
 491 (i.e., co-eruptive degassing; see Section 2), and thus we expect \bar{S} to be dominated by de-
 492 compressional degassing and hence much higher than predicted for chamber degassing
 493 alone.

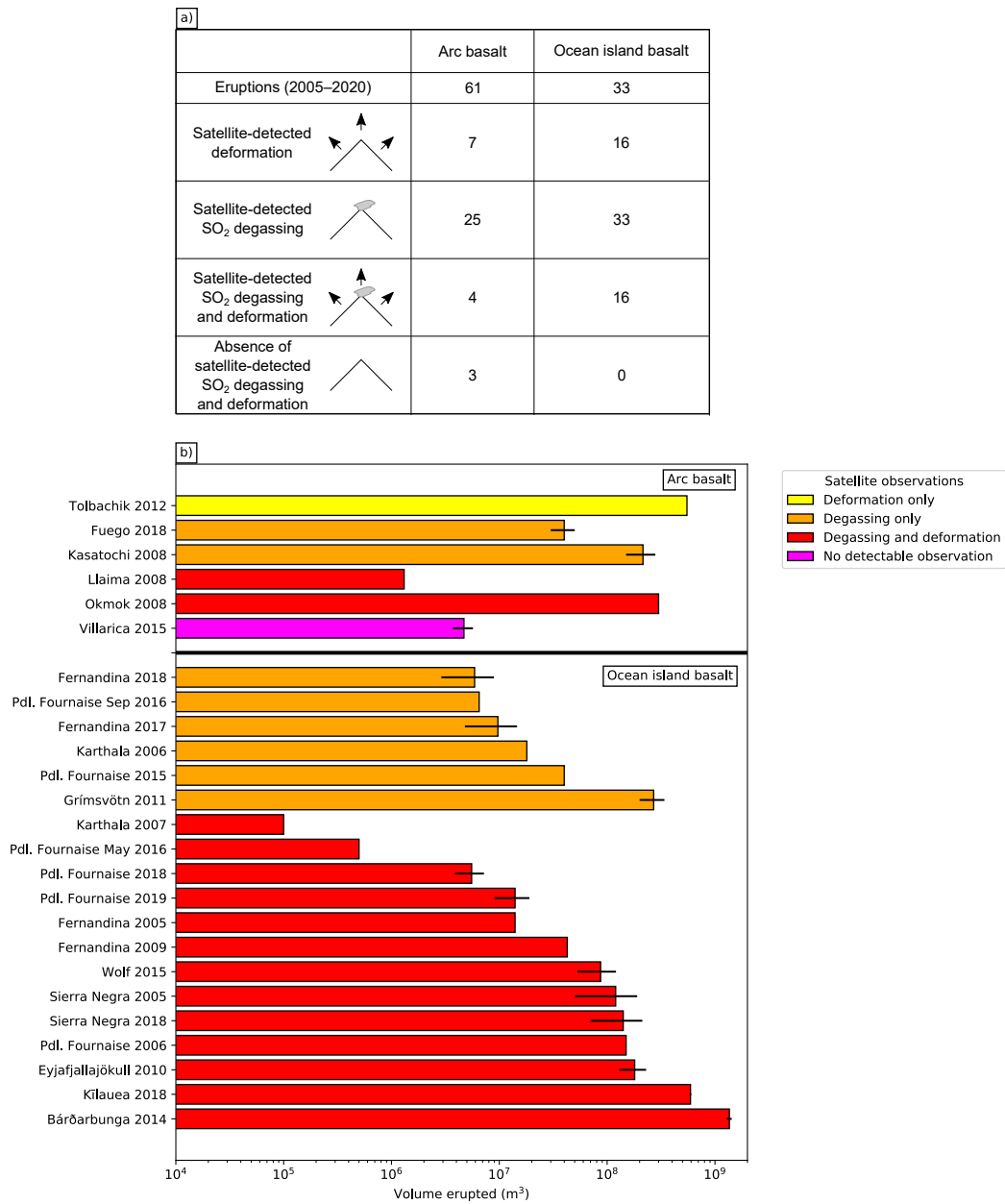
494 5.2 Comparison to Satellite Observations

495 In this section, we compare the magma properties predicted by the thermodynamic
 496 framework with observations of eruptions to understand published catalogues of volcanic
 497 deformation and degassing.

498 5.2.1 Data Compilation

499 Observations of volcanic deformation and SO_2 degassing during an eruption de-
 500 pend on both the properties of the magma and crust. Here we compiled deformation and
 501 SO_2 degassing data for 94 volcanic eruptions during the satellite era (2005-2020) to un-
 502 derstand how theoretical estimates from thermodynamic modelling compare with observed
 503 eruptions (Supplementary Table 1). The primary magma composition and the dates for
 504 past eruptions are drawn from the Global Volcanism Program (2013). The compilation
 505 only considers volcanoes of basaltic composition. For eruptions with poorly constrained
 506 starting or ending dates, particularly for long-lived eruptions, we select the dates at which
 507 significant eruptions occur such as the the 2018 eruptions of Kilauea, Ambrym and Fuego
 508 (e.g., Neal et al., 2019; Hamling et al., 2019; Naismith et al., 2019).

509 We compile 23 episodes of pre- and co-eruptive deformation detected with InSAR
 510 from the published catalogues of Biggs and Pritchard (2017) and Ebmeier et al. (2018)
 511 and 58 satellite observations of SO_2 degassing from individual studies (Supplementary
 512 Table 1), published catalogues (Carn et al., 2016, 2017) and Global Volcanism Program
 513 (2013). For eruptions that are less well studied (e.g., Chikurachki, Pagan, Semisopchnoi),



514 evidence for SO₂ degassing are crosschecked with the Global Sulphur Dioxide Monitor-
515 ing homepage (<https://so2.gsfc.nasa.gov/>). Persistently degassing volcanoes (e.g., Shishaldin,
516 Saunders, Korovin), including those whose emissions can be detected by satellites (e.g.,
517 Masaya, Miyakejima, Telica) (Carn et al., 2017), and submarine eruptions (e.g., May-
518 otte, Axial Seamount, Bristol Island) are not considered in this compilation. We also do
519 not consider volcanoes that have approximately equal passive and eruptive SO₂ degassing
520 regime such as Manam and Ulawun (Carn et al., 2016). We do, however, include erup-
521 tions that are significantly explosive (e.g., 2018 eruptions of Ambrym and Kīlauea).

522 We find that observations of deformation and SO₂ degassing are not available for
523 every eruption despite similar erupted volume or volcano (Figure 8b). In fact, there is
524 no clear correlation between satellite observations and erupted volume, consistent with
525 previous studies (Kilbride et al., 2016), largely due to the challenges in volcano moni-
526 toring such as atmospheric noise, ice cover, or limitations in satellite sensors (e.g., OMI
527 row anomaly for the 2012 eruption of Tolbachik). For example, satellite sensors could
528 not measure the deformation associated with the 2011 eruption of Grimsvötn due to ice
529 cover. Similarly, satellite measurement of SO₂ degassing is not available for the 2012-
530 2013 eruption of Tolbachik, despite being one of the most voluminous arc basalt erup-
531 tions (Belousov et al., 2015), due to the OMI row anomaly (see [https://so2.gsfc.nasa.gov/
532 pix/daily/1112/kamchat_1112z.html](https://so2.gsfc.nasa.gov/pix/daily/1112/kamchat_1112z.html)).

533 Overall, deformation was detected at 25% of eruptions (23/94) and SO₂ degassing
534 at 62% of eruptions (58/94)(Supplementary Table 1). A similar analysis conducted by
535 Furtney et al. (2018) uses multiple satellite data spanning 1978-2016 to synthesise ob-
536 servations of volcanic deformation and degassing. Their study yielded similar results to
537 ours: of the 250 volcanic eruptions between 1978-2016, 28% of eruptions have satellite
538 observations of volcanic deformation, and SO₂ degassing is observed at 67% of eruptions
539 (Furtney et al., 2018). The slightly higher proportion of volcanoes with satellite-detected
540 deformation and degassing analysed by Furtney et al. (2018) is likely caused by the in-
541 clusion of pre- and post-eruptive observations. The overall proportion of satellite obser-
542 vations of volcanic deformation and SO₂ degassing appears to be fairly consistent be-
543 tween studies.

544 **5.2.2 Comparison between tectonic settings**

545 Our compilation shows that co-eruptive deformation has been observed at 48% of
546 eruptions involving ocean island basalts (16/33), while only 11% of arc basalt eruptions
547 had observed deformation (7/61) (Supplementary Table 1; Figure 8a). The lower frequency
548 of detectable deformation at arc basalt eruptions can be attributed to the higher volatile
549 contents of arc magmas, which our thermodynamic model predicts will increase magma
550 compressibility and reduce surface deformation (Figure 7f-h). Systematic satellite ob-
551 servations of deformation spanning 1992-2010 analysed by Biggs et al. (2014) shows that
552 the proportion of deforming volcanoes that erupted is higher for volcanoes in hotspot
553 setting (66%; ocean island) as compared to those in subduction setting (53%; arc). For
554 example, there are few InSAR observations from the Central American Volcanic Arc, where
555 parental melts are water-rich (Ebmeier et al., 2013b; Wallace, 2005). Although this is
556 an indirect comparison, the study agrees well with our results that observations of vol-
557 canic deformation are dominated by ocean island basalt eruptions. However, we note that
558 other potential factors may also contribute to the lack of detectable deformation at vol-
559 canoes, independently or collectively (e.g. the rate of magma recharge, chamber geom-
560 etry, depth of magma storage, viscoelastic crustal rheology, an open conduit, pre-eruptive
561 degassing, atmospheric noise (Ebmeier et al., 2013b, 2013a; Chaussard et al., 2013; Head
562 et al., 2019; Yip et al., 2019)) meaning that the models are very uncertain.

563 Volcanic SO₂ degassing was observed at all 33 ocean island basalt eruptions in our
564 compilation but at only 41% of the arc basalt eruptions (25/61) (Supplementary Table
565 1; Figure 8a). While the higher magmatic volatile content of arc basalts might be ex-
566 pected to produce a higher detection rate (Figure 7c), the high rate of detection at ocean
567 island basalt can be attributed to co-eruptive degassing. Conversely, the explosive na-
568 ture of the arc basalt eruptions may mean there is there is no co-eruptive degassing and
569 the only volatiles released are those in equilibrium at chamber depth. Additionally, tech-
570 nical difficulties in spectrometers, such as the ‘row anomaly’ in OMI that obscures the
571 spectrometer’s field of view (e.g., 2019 eruption of Klyuchevskoy, 2012 eruption of Tol-
572 bachik, 2010 eruption of Manam) prevents routine volcano monitoring.

573 We find that eruptions that have both satellite observations of volcanic deforma-
574 tion and degassing to be higher for ocean island basalt (16/33) as compared to arc basalt
575 (4/61) (Figure 8a). Similarly, all ocean island basalts eruptions have been observed by
576 at least one satellite sensor, while 3 of the 61 arc basalt eruptions were not detected by

577 either sensors. The lack of satellite observations for arc basalt eruptions highlights the
 578 difficulties in monitoring explosive eruptions with high magmatic volatile contents and
 579 thus compressible magmas (Huppert & Woods, 2002; Rivalta & Segall, 2008; Kilbride
 580 et al., 2016), and volcanoes with deep magma storage depth (Moran et al., 2006; Ebmeier
 581 et al., 2013b).

582 Finally, we further analyse 25 eruptions with erupted volume $\geq 1 \times 10^5 \text{ m}^3$ (Fig-
 583 ure 8b) to ensure comparable detection thresholds. All 19 ocean island basalt eruptions
 584 with erupted volume $\geq 1 \times 10^5 \text{ m}^3$ have satellite observations of SO_2 degassing of which
 585 13 have deformation measured by satellites (Figure 8b). For the case of arc basalt erup-
 586 tions, we find no clear correlation between erupted volume $\geq 1 \times 10^5 \text{ m}^3$ and satellite ob-
 587 servations of SO_2 degassing and deformation (Figure 8b), in agreement with the wider
 588 catalogue and previous studies (Kilbride et al., 2016). This highlights the challenges for
 589 satellites to detect surface deformation, particularly for more evolved arc basaltic erup-
 590 tions that are more compressible.

591 In summary, the thermodynamic framework and satellite observations of deforma-
 592 tion agree well with each other such that volcanic deformation of volatile-poor ocean is-
 593 land basalt are more likely to be detected by satellites as compared to volatile-rich arc
 594 basalt (Figure 7g-h; Figure 8a). This is because volatile-rich arc basalts are highly com-
 595 pressible, which results in muted surface deformation. Predictions of SO_2 degassing from
 596 our thermodynamic framework shows that volatile-rich arc basalts have greater SO_2 de-
 597 gassing, yet satellite observations show otherwise (Figure 7c; Figure 8a). We note that
 598 while the water content in arc basalts is two times greater than that of ocean island basalts,
 599 the sulfur content in basalts from both tectonic settings are similar (Table 3). The re-
 600 lationship between volatile content in basalts and satellite detections of SO_2 degassing
 601 suggests that eruption style plays a greater role than the volatile content of basalts in
 602 determining volcanic SO_2 .

603 **6 Discussion and Conclusion**

604 The thermodynamic framework presented in this study provides a quantitative link
 605 between observations of volcanic deformation and degassing. The framework is used to
 606 explore the sensitivity of magma properties to several controlling parameters (magmatic
 607 H_2O , magmatic CO_2 , magmatic S, oxygen fugacity f_{O_2} , crustal shear modulus μ , and
 608 chamber geometry), which vary systematically between tectonic setting. We demonstrated

609 that the results from thermodynamic models can be used to to calculate three key ob-
610 servables, SO₂ emissions, co-eruptive volume change and maximum vertical displacement,
611 all of which are normalised by the erupted volume, and the dependence of these observ-
612 ables on pre-eruptive magmatic and chamber conditions. The conclusions of this study
613 are as follow:

- 614 1. Magmas with high magmatic H₂O content have high SO₂ gas emissions and a high
615 magma compressibility, which results in muted surface deformation during erup-
616 tions. While high magmatic CO₂ has little effect on SO₂ gas emissions, it increases
617 magma compressibility and thus reduces surface deformation. Varying oxygen fu-
618 gacity from NNO-1 to NNO+1 and increasing magmatic S increase sulfur gas emis-
619 sions but has little effect magma compressibility.
- 620 2. Volcanoes with volatile-rich magma but stiff host rock have high magma compress-
621 ibility and low chamber compressibility, respectively, which leads to more muted
622 ground deformation during eruptions when compared to volcanoes that have volatile-
623 poor magma and compliant host rock.
- 624 3. The volatile content of magmas varies between tectonic settings and this influences
625 both ground deformation and degassing during eruptions. Arc basalts, which tend
626 to have higher magmatic volatile contents, have more muted ground deformation
627 than ocean island basalts, which is reflected in observations over the satellite era.

628 Our thermodynamic framework has the potential to link observations of volcanic
629 deformation and degassing. However, there are caveats to this framework, such as 1) magma
630 chambers with different geometries exhibit different magnitude of deformation (e.g., Gud-
631 mundsson, 2008; Amoroso & Crescentini, 2009; Anderson & Segall, 2011), 2) the mag-
632 nitude of deformation may be influenced by viscoelastic responses of the crust (e.g., Hickey
633 et al., 2013; Head et al., 2019; Gottsmann et al., 2020), 3) both magma composition and
634 pre- and co-eruption gas segregation affect observations of deformation and degassing
635 (e.g., Wallace, 2005; Edmonds et al., 2014; Edmonds & Woods, 2018), and 4) it is dif-
636 ficult to differentiate which parameter has the biggest influence on the observations of
637 each eruption. Additional complexities listed above are not introduced to this framework
638 as the goal of this study is to reconcile observations of volcanic deformation and degassing.

639 While the simplicity of this model is useful for considering general trends, oversim-
640 plification reduces the applicability to individual eruptions. The assumption of a typ-

641 ical crustal shear modulus may be appropriate for the sensitivity tests, but it is not ap-
 642 plicable to all volcanoes. Similarly, we did not consider the effects of pre-eruptive gas
 643 segregation on magma properties, which in reality could affect co-eruptive observations
 644 (e.g., Wallace, 2001; Huppert & Woods, 2002; Rivalta & Segall, 2008). In practice, more
 645 parameters are needed to be considered to provide realism (Masterlark, 2003).

646 With results from the thermodynamic framework, we have developed a better un-
 647 derstanding of the effects of magmatic volatile content and crustal compressibility on the
 648 physicochemical properties of magma. Our future work will explore pre-eruptive gas seg-
 649regation processes such as gas accumulation and degassing to understand its implications
 650 on observations of volcanic deformation and degassing. Future studies should refine this
 651 framework for specific circumstances to resolve additional complexities.

652 **Acknowledgments**

653 This research is supported by the NERC-BGS Centre for the Observation and Modelling
 654 of Earthquakes Volcanoes and Tectonics (COMET) for SY, JB and ME. SY and JB are
 655 funded by the Leverhulme Trust, and PL acknowledges funding from the Embiricos Trust
 656 Scholarship from Jesus College, Cambridge.

657 **References**

- 658 Albino, F., Biggs, J., & Syahbana, D. K. (2019, 12). Dyke intrusion between neigh-
 659 bouring arc volcanoes re- sponsible for 2017 pre-eruptive seismic swarm at
 660 Agung, Bali. *Nature Communications*, *10*(1), 748. Retrieved from [http://](http://www.nature.com/articles/s41467-019-08564-9)
 661 www.nature.com/articles/s41467-019-08564-9[http://dx.doi.org/](http://dx.doi.org/10.1038/s41467-019-08564-9)
 662 [10.1038/s41467-019-08564-9](http://dx.doi.org/10.1038/s41467-019-08564-9) doi: 10.1038/s41467-019-08564-9
- 663 Amoruso, A., & Crescentini, L. (2009, 2). Shape and volume change of pressurized
 664 ellipsoidal cavities from deformation and seismic data. *Journal of Geophysical*
 665 *Research*, *114*(B2), B02210. Retrieved from [http://doi.wiley.com/10.1029/](http://doi.wiley.com/10.1029/2008JB005946)
 666 [2008JB005946](http://doi.wiley.com/10.1029/2008JB005946) doi: 10.1029/2008JB005946
- 667 Anderson, K., & Segall, P. (2011, 7). Physics-based models of ground deformation
 668 and extrusion rate at effusively erupting volcanoes. *Journal of Geophysical Re-*
 669 *search: Solid Earth*, *116*(7), 1–20. Retrieved from [http://doi.wiley.com/10](http://doi.wiley.com/10.1029/2010JB007939)
 670 [.1029/2010JB007939](http://doi.wiley.com/10.1029/2010JB007939) doi: 10.1029/2010JB007939
- 671 Bachmann, O., & Bergantz, G. W. (2006, 1). Gas percolation in upper-crustal silicic

- 672 crystal mushes as a mechanism for upward heat advection and rejuvenation of
 673 near-solidus magma bodies. *Journal of Volcanology and Geothermal Research*,
 674 *149*(1-2), 85–102. doi: 10.1016/J.JVOLGEORES.2005.06.002
- 675 Belousov, A., Belousova, M., Edwards, B., Volynets, A., & Melnikov, D. (2015, 12).
 676 Overview of the precursors and dynamics of the 2012-13 basaltic fissure erup-
 677 tion of Tolbachik Volcano, Kamchatka, Russia. *Journal of Volcanology and*
 678 *Geothermal Research*, *307*, 22–37. doi: 10.1016/j.jvolgeores.2015.06.013
- 679 Biggs, J., Ebmeier, S. K., Aspinall, W. P., Lu, Z., Pritchard, M. E., Sparks, R. S.,
 680 & Mather, T. A. (2014). Global link between deformation and volcanic
 681 eruption quantified by satellite imagery. *Nature Communications*, *5*. doi:
 682 10.1038/ncomms4471
- 683 Biggs, J., & Pritchard, M. E. (2017). Global volcano monitoring: What does it mean
 684 when volcanoes deform? *Elements*, *13*(1), 17–22. doi: 10.2113/gselements.13.1
 685 .17
- 686 Biggs, J., & Wright, T. J. (2020, 12). *How satellite InSAR has grown from op-*
 687 *portunistic science to routine monitoring over the last decade* (Vol. 11)
 688 (No. 1). Nature Research. Retrieved from [https://doi.org/10.1038/](https://doi.org/10.1038/s41467-020-17587-6)
 689 [s41467-020-17587-6](https://doi.org/10.1038/s41467-020-17587-6) doi: 10.1038/s41467-020-17587-6
- 690 Burgisser, A., Alletti, M., & Scaillet, B. (2015). Simulating the behavior of volatiles
 691 belonging to the C-O-H-S system in silicate melts under magmatic condi-
 692 tions with the software D-Compress. *Computers and Geosciences*. doi:
 693 10.1016/j.cageo.2015.03.002
- 694 Burgisser, A., Chevalier, L., Gardner, J. E., & Castro, J. M. (2017, 7). The per-
 695 colation threshold and permeability evolution of ascending magmas. *Earth and*
 696 *Planetary Science Letters*, *470*, 37–47. Retrieved from [http://dx.doi.org/10](http://dx.doi.org/10.1016/j.epsl.2017.04.023)
 697 [.1016/j.epsl.2017.04.023](http://dx.doi.org/10.1016/j.epsl.2017.04.023) doi: 10.1016/j.epsl.2017.04.023
- 698 Candela, P. A. (1997, 12). A Review of Shallow, Ore-related Granites: Textures,
 699 Volatiles, and Ore Metals. *Journal of Petrology*, *38*(12), 1619–1633. Retrieved
 700 from <https://academic.oup.com/petrology/article/38/12/1619/1604064>
 701 doi: 10.1093/PETROJ/38.12.1619
- 702 Carboni, E., Grainger, R. G., Mather, T. A., Pyle, D. M., Thomas, G. E., Siddans,
 703 R., ... Balis, D. (2016, 4). The vertical distribution of volcanic SO₂ plumes
 704 measured by IASI. *Atmospheric Chemistry and Physics*, *16*(7), 4343–4367.

705 doi: 10.5194/acp-16-4343-2016

706 Carmichael, I. S., & Ghiorso, M. S. (1986, 6). Oxidation-reduction relations in basic
 707 magma: a case for homogeneous equilibria. *Earth and Planetary Science Let-*
 708 *ters*, 78(2-3), 200–210. doi: 10.1016/0012-821X(86)90061-0

709 Carn, S. A., Clarisse, L., & Prata, A. J. (2016, 2). *Multi-decadal satellite measure-*
 710 *ments of global volcanic degassing* (Vol. 311). Elsevier B.V. doi: 10.1016/j
 711 .jvolgeores.2016.01.002

712 Carn, S. A., Fioletov, V. E., Mclinden, C. A., Li, C., & Krotkov, N. A. (2017, 3).
 713 A decade of global volcanic SO₂ emissions measured from space. *Scientific*
 714 *Reports*, 7(1), 1–12. Retrieved from [https://www.nature.com/articles/](https://www.nature.com/articles/srep44095)
 715 [srep44095](https://www.nature.com/articles/srep44095) doi: 10.1038/srep44095

716 Chaussard, E., & Amelung, F. (2014, 4). Regional controls on magma ascent and
 717 storage in volcanic arcs. *Geochemistry, Geophysics, Geosystems*, 15(4), 1407–
 718 1418. Retrieved from <http://doi.wiley.com/10.1002/2013GC005216> doi: 10
 719 .1002/2013GC005216

720 Chaussard, E., Amelung, F., & Aoki, Y. (2013). Characterization of open and closed
 721 volcanic systems in Indonesia and Mexico using InSAR time series. *Journal of*
 722 *Geophysical Research: Solid Earth*. doi: 10.1002/jgrb.50288

723 Collins, S. J., Pyle, D. M., & Maclennan, J. (2009, 6). Melt inclusions track pre-
 724 eruption storage and dehydration of magmas at Etna. *Geology*, 37(6), 571–
 725 574. doi: 10.1130/G30040A.1

726 Colombier, M., Wadsworth, F. B., Scheu, B., Vasseur, J., Dobson, K. J., Cáceres,
 727 F., . . . Dingwell, D. B. (2020, 4). In situ observation of the percolation
 728 threshold in multiphase magma analogues. *Bulletin of Volcanology*, 82(4),
 729 1–15. Retrieved from <https://doi.org/10.1007/s00445-020-1370-1> doi:
 730 10.1007/s00445-020-1370-1

731 Coppola, D., Laiolo, M., Cigolini, C., Massimetti, F., Delle Donne, D., Ripepe, M.,
 732 . . . William, R. (2020, 1). Thermal Remote Sensing for Global Volcano Moni-
 733 toring: Experiences From the MIROVA System. *Frontiers in Earth Science*, 7,
 734 362. doi: 10.3389/FEART.2019.00362/BIBTEX

735 Delgado, F., Pritchard, M. E., Ebmeier, S., González, P., & Lara, L. (2017,
 736 9). Recent unrest (2002–2015) imaged by space geodesy at the highest
 737 risk Chilean volcanoes: Villarrica, Llaima, and Calbuco (Southern An-

- 738 des). *Journal of Volcanology and Geothermal Research*, 344, 270–288. doi:
739 10.1016/j.jvolgeores.2017.05.020
- 740 Duan, X. (2014). A general model for predicting the solubility behavior of
741 H₂O-CO₂ fluids in silicate melts over a wide range of pressure, tempera-
742 ture and compositions. *Geochimica et Cosmochimica Acta*, 125, 582–609.
743 Retrieved from <http://dx.doi.org/10.1016/j.gca.2013.10.018> doi:
744 10.1016/j.gca.2013.10.018
- 745 Ebmeier, S. K., Andrews, B. J., Araya, M. C., Arnold, D. W. D., Biggs, J., Cooper,
746 C., ... Williamson, J. L. (2018, 12). Synthesis of global satellite observations
747 of magmatic and volcanic deformation: implications for volcano monitoring &
748 the lateral extent of magmatic domains. *Journal of Applied Volcanology*, 7(1),
749 1–26. Retrieved from [https://appliedvolc.springeropen.com/articles/](https://appliedvolc.springeropen.com/articles/10.1186/s13617-018-0071-3)
750 [10.1186/s13617-018-0071-3](https://appliedvolc.biomedcentral.com/track/pdf/10.1186/s13617-018-0071-3) doi: 10.1186/s13617-018-0071-3
- 751 Ebmeier, S. K., Biggs, J., Mather, T. A., & Amelung, F. (2013a). Applicability of
752 InSAR to tropical volcanoes: insights from Central America. *Geological Soci-*
753 *ety, London, Special Publications*. doi: 10.1144/SP380.2
- 754 Ebmeier, S. K., Biggs, J., Mather, T. A., & Amelung, F. (2013b, 5). *On the*
755 *lack of InSAR observations of magmatic deformation at Central Ameri-*
756 *can volcanoes* (Vol. 118) (No. 5). Blackwell Publishing Ltd. Retrieved
757 from [https://agupubs.onlinelibrary.wiley.com/doi/full/10.1002/](https://agupubs.onlinelibrary.wiley.com/doi/full/10.1002/jgrb.50195)
758 [jgrb.50195](https://agupubs.onlinelibrary.wiley.com/doi/abs/10.1002/jgrb.50195)[https://agupubs.onlinelibrary.wiley.com/doi/abs/10.1002/](https://agupubs.onlinelibrary.wiley.com/doi/abs/10.1002/jgrb.50195)
759 [jgrb.50195](https://agupubs.onlinelibrary.wiley.com/doi/10.1002/jgrb.50195)[https://agupubs.onlinelibrary.wiley.com/doi/10.1002/](https://agupubs.onlinelibrary.wiley.com/doi/10.1002/jgrb.50195)
760 [jgrb.50195](https://agupubs.onlinelibrary.wiley.com/doi/10.1002/jgrb.50195) doi: 10.1002/jgrb.50195
- 761 Ebmeier, S. K., Elliott, J. R., Nocquet, J. M., Biggs, J., Mothes, P., Jarrín, P.,
762 ... Samsonov, S. V. (2016, 9). Shallow earthquake inhibits unrest near
763 Chiles–Cerro Negro volcanoes, Ecuador–Colombian border. *Earth and Plane-*
764 *tary Science Letters*, 450, 283–291. doi: 10.1016/j.epsl.2016.06.046
- 765 Edmonds, M., Cashman, K. V., Holness, M., & Jackson, M. (2019). Architecture
766 and dynamics of magma reservoirs. *Philosophical Transactions of the Royal So-*
767 *ciety A: Mathematical, Physical and Engineering Sciences*, 377(2139). doi: 10
768 .1098/rsta.2018.0298
- 769 Edmonds, M., Humphreys, M. C., Hauri, E. H., Herd, R. A., Wadge, G., Rawson,

- 771 H., ... Guida, R. (2014, 1). Pre-eruptive vapour and its role in controlling
 772 eruption style and longevity at Soufrière Hills Volcano. *Geological Society*
 773 *Memoir*, 39(1), 291–315. doi: 10.1144/M39.16
- 774 Edmonds, M., Mather, T. A., & Liu, E. J. (2018). A distinct metal fingerprint in
 775 arc volcanic emissions. *Nature Geoscience*, 11(10), 790–794. Retrieved from
 776 <http://dx.doi.org/10.1038/s41561-018-0214-5> doi: 10.1038/s41561-018-
 777 -0214-5
- 778 Edmonds, M., & Woods, A. W. (2018). Exsolved volatiles in magma reser-
 779 voirs. *Journal of Volcanology and Geothermal Research*, 368, 13–30. Re-
 780 trieved from <https://doi.org/10.1016/j.jvolgeores.2018.10.018> doi:
 781 10.1016/j.jvolgeores.2018.10.018
- 782 Fialko, Y., Simons, M., & Agnew, D. (2001, 8). The complete (3-D) surface dis-
 783 placement field in the epicentral area of the 1999 Mw 7.1 Hector Mine earth-
 784 quake, California, from space geodetic observations. *Geophysical Research*
 785 *Letters*, 28(16), 3063–3066. Retrieved from [https://agupubs.onlinelibrary](https://agupubs.onlinelibrary.wiley.com/doi/full/10.1029/2001GL013174)
 786 [.wiley.com/doi/full/10.1029/2001GL013174](https://agupubs.onlinelibrary.wiley.com/doi/full/10.1029/2001GL013174)[https://agupubs](https://agupubs.onlinelibrary.wiley.com/doi/abs/10.1029/2001GL013174)
 787 [.onlinelibrary.wiley.com/doi/abs/10.1029/2001GL013174](https://agupubs.onlinelibrary.wiley.com/doi/abs/10.1029/2001GL013174)[https://](https://agupubs.onlinelibrary.wiley.com/doi/10.1029/2001GL013174)
 788 agupubs.onlinelibrary.wiley.com/doi/10.1029/2001GL013174 doi:
 789 10.1029/2001GL013174
- 790 Furtney, M. A., Pritchard, M. E., Biggs, J., Carn, S. A., Ebmeier, S. K., Jay, J. A.,
 791 ... Reath, K. A. (2018, 10). Synthesizing multi-sensor, multi-satellite, multi-
 792 decadal datasets for global volcano monitoring. *Journal of Volcanology and*
 793 *Geothermal Research*, 365, 38–56. doi: 10.1016/j.jvolgeores.2018.10.002
- 794 Gaillard, F., & Scaillet, B. (2014, 10). A theoretical framework for volcanic de-
 795 gassing chemistry in a comparative planetology perspective and implications
 796 for planetary atmospheres. *Earth and Planetary Science Letters*, 403, 307–316.
 797 doi: 10.1016/j.epsl.2014.07.009
- 798 Ge, C., Wang, J., Carn, S., Yang, K., Ginoux, P., & Krotkov, N. (2016, 4). Satellite-
 799 based global volcanic SO₂ emissions and sulfate direct radiative forcing during
 800 2005-2012. *Journal of Geophysical Research*, 121(7), 3446–3464. Retrieved
 801 from [https://agupubs.onlinelibrary.wiley.com/doi/full/10.1002/](https://agupubs.onlinelibrary.wiley.com/doi/full/10.1002/2015JD023134)
 802 [2015JD023134](https://agupubs.onlinelibrary.wiley.com/doi/abs/10.1002/2015JD023134)[https://agupubs.onlinelibrary.wiley.com/doi/abs/](https://agupubs.onlinelibrary.wiley.com/doi/abs/10.1002/2015JD023134)
 803 [10.1002/2015JD023134](https://agupubs.onlinelibrary.wiley.com/doi/10.1002/2015JD023134)[https://agupubs.onlinelibrary.wiley.com/doi/](https://agupubs.onlinelibrary.wiley.com/doi/10.1002/2015JD023134)

- 804 10.1002/2015JD023134 doi: 10.1002/2015JD023134
- 805 Girona, T., Costa, F., Newhall, C., & Taisne, B. (2014, 12). On depressurization
806 of volcanic magma reservoirs by passive degassing. *Journal of Geophysical Re-*
807 *search: Solid Earth*, 119(12), 8667–8687. Retrieved from [http://doi.wiley](http://doi.wiley.com/10.1002/2014JB011368)
808 [.com/10.1002/2014JB011368](http://doi.wiley.com/10.1002/2014JB011368) doi: 10.1002/2014JB011368
- 809 Gottsmann, J., Biggs, J., Lloyd, R., Biranhu, Y., & Lewi, E. (2020, 4). Ductility and
810 compressibility accommodate high magma flux beneath a silicic continental rift
811 caldera: Insights from Corbetti caldera (Ethiopia). *Geochemistry, Geophysics,*
812 *Geosystems*, 21(4), e2020GC008952. doi: 10.1029/2020gc008952
- 813 Gualda, G. A., Ghiorso, M. S., Lemons, R. V., & Carley, T. L. (2012, 5). Rhyolite-
814 MELTS: a Modified Calibration of MELTS Optimized for Silica-rich, Fluid-
815 bearing Magmatic Systems. *Journal of Petrology*, 53(5), 875–890. Retrieved
816 from <https://academic.oup.com/petrology/article/53/5/875/1527627>
817 doi: 10.1093/PETROLOGY/EGR080
- 818 Gudmundsson, A. (2005, 9). The effects of layering and local stresses in composite
819 volcanoes on dyke emplacement and volcanic hazards. *Comptes Rendus - Geo-*
820 *science*, 337(13), 1216–1222. doi: 10.1016/j.crte.2005.07.001
- 821 Gudmundsson, A. (2008, 1). *Chapter 8 Magma-Chamber Geometry, Fluid Trans-*
822 *port, Local Stresses and Rock Behaviour During Collapse Caldera Formation*
823 (Vol. 10) (No. C). Elsevier. doi: 10.1016/S1871-644X(07)00008-3
- 824 Hamling, I. J., Cevuard, S., & Garaebiti, E. (2019, 5). Large-Scale Drainage of a
825 Complex Magmatic System: Observations From the 2018 Eruption of Am-
826 brym Volcano, Vanuatu. *Geophysical Research Letters*, 46(9), 4609–4617. doi:
827 10.1029/2019GL082606
- 828 Hautmann, S., Gottsmann, J., Sparks, R. S. J., Mattioli, G. S., Sacks, I. S., &
829 Strutt, M. H. (2010, 9). Effect of mechanical heterogeneity in arc crust on
830 volcano deformation with application to Soufrière Hills Volcano, Montserrat,
831 West Indies. *Journal of Geophysical Research: Solid Earth*, 115(B9), 9203.
832 Retrieved from [https://onlinelibrary.wiley.com/doi/full/10.1029/](https://onlinelibrary.wiley.com/doi/full/10.1029/2009JB006909)
833 [https://onlinelibrary.wiley.com/doi/abs/10.1029/](https://onlinelibrary.wiley.com/doi/abs/10.1029/2009JB006909)
834 [https://agupubs.onlinelibrary.wiley.com/doi/10.1029/](https://agupubs.onlinelibrary.wiley.com/doi/10.1029/2009JB006909)
835 [2009JB006909](https://agupubs.onlinelibrary.wiley.com/doi/10.1029/2009JB006909) doi: 10.1029/2009JB006909
- 836 Head, M., Hickey, J., Gottsmann, J., & Fournier, N. (2019, 8). The Influ-

- 837 ence of Viscoelastic Crustal Rheologies on Volcanic Ground Deforma-
838 tion: Insights From Models of Pressure and Volume Change. *Journal of*
839 *Geophysical Research: Solid Earth*, 124(8), 8127–8146. Retrieved from
840 <https://onlinelibrary.wiley.com/doi/10.1029/2019JB017832> doi:
841 10.1029/2019JB017832
- 842 Heap, M. J., Villeneuve, M., Albino, F., Farquharson, J. I., Brothelande, E.,
843 Amelung, F., . . . Baud, P. (2020, 1). Towards more realistic values of elas-
844 tic moduli for volcano modelling. *Journal of Volcanology and Geothermal*
845 *Research*, 390, 106684. doi: 10.1016/j.jvolgeores.2019.106684
- 846 Hickey, J., Gottsmann, J., & Del Potro, R. (2013, 3). The large-scale sur-
847 face uplift in the Altiplano-Puna region of Bolivia: A parametric study
848 of source characteristics and crustal rheology using finite element analy-
849 sis. *Geochemistry, Geophysics, Geosystems*, 14(3), 540–555. Retrieved
850 from [https://agupubs.onlinelibrary.wiley.com/doi/full/10.1002/](https://agupubs.onlinelibrary.wiley.com/doi/full/10.1002/ggge.20057)
851 [ggge.20057https://agupubs.onlinelibrary.wiley.com/doi/abs/10.1002/](https://agupubs.onlinelibrary.wiley.com/doi/abs/10.1002/ggge.20057)
852 [ggge.20057https://agupubs.onlinelibrary.wiley.com/doi/10.1002/](https://agupubs.onlinelibrary.wiley.com/doi/10.1002/ggge.20057)
853 [ggge.20057](https://agupubs.onlinelibrary.wiley.com/doi/10.1002/ggge.20057) doi: 10.1002/ggge.20057
- 854 Huppert, H. E., & Woods, A. W. (2002). The role of volatiles in magma chamber
855 dynamics. *Nature*, 420(6915), 493–495. doi: 10.1038/nature01211
- 856 Kilbride, B. M. C., Edmonds, M., & Biggs, J. (2016, 12). Observing eruptions of
857 gas-rich compressible magmas from space. *Nature Communications*, 7(1), 1–8.
858 Retrieved from <http://dx.doi.org/10.1038/ncomms13744>[www.nature.com/](http://www.nature.com/naturecommunications)
859 [naturecommunications](http://www.nature.com/naturecommunications) doi: 10.1038/ncomms13744
- 860 Liggins, P., Jordan, S., Rimmer, P. B., & Shorttle, O. (2021, 11). Growth and evolu-
861 tion of secondary volcanic atmospheres: I. Identifying the geological character
862 of warm rocky planets. *arXiv*. Retrieved from [https://arxiv.org/abs/](https://arxiv.org/abs/2111.05161v1)
863 2111.05161v1
- 864 Liggins, P., Shorttle, O., & Rimmer, P. B. (2020, 11). Can volcanism build
865 hydrogen-rich early atmospheres? *Earth and Planetary Science Letters*, 550,
866 116546. doi: 10.1016/J.EPSL.2020.116546
- 867 Lindoo, A., Larsen, J. F., Cashman, K. V., & Oppenheimer, J. (2017, 9). Crys-
868 tal controls on permeability development and degassing in basaltic andesite
869 magma. *Geology*, 45(9), 831–834. Retrieved from <https://imagej.nih.gov>

870 doi: 10.1130/G39157.1

871 Lowenstern, J. B. (1994, 10). Dissolved volatile concentrations in an ore-forming
872 magma. *Geology*, 22(10), 893–896. doi: 10.1130/0091-7613(1994)022<0893:
873 dvciao>2.3.co;2

874 Masterlark, T. (2003, 11). Finite element model predictions of static deforma-
875 tion from dislocation sources in a subduction zone: Sensitivities to homo-
876 geneous, isotropic, Poisson-solid, and half-space assumptions. *Journal of*
877 *Geophysical Research: Solid Earth*, 108(B11), 2540. Retrieved from [https://](https://onlinelibrary.wiley.com/doi/full/10.1029/2002JB002296)
878 onlinelibrary.wiley.com/doi/full/10.1029/2002JB002296[https://](https://onlinelibrary.wiley.com/doi/abs/10.1029/2002JB002296)
879 onlinelibrary.wiley.com/doi/abs/10.1029/2002JB002296[https://](https://agupubs.onlinelibrary.wiley.com/doi/10.1029/2002JB002296)
880 agupubs.onlinelibrary.wiley.com/doi/10.1029/2002JB002296 doi:
881 10.1029/2002JB002296

882 Mogi, K. (1958). Relations between the eruptions of various volcanoes and the
883 deformations of the ground surfaces around them. *Bulletin of the Earthquake*
884 *Research Institute*, 36, 99–134. Retrieved from [http://repository.dl.itc](http://repository.dl.itc.u-tokyo.ac.jp/dspace/handle/2261/11909%5Cnpapers://8461d6ef-4184-45b2-aa3d-395291ea6525/Paper/p3868)
885 [.u-tokyo.ac.jp/dspace/handle/2261/11909%5Cnpapers://8461d6ef-4184](http://repository.dl.itc.u-tokyo.ac.jp/dspace/handle/2261/11909%5Cnpapers://8461d6ef-4184-45b2-aa3d-395291ea6525/Paper/p3868)
886 [-45b2-aa3d-395291ea6525/Paper/p3868](http://repository.dl.itc.u-tokyo.ac.jp/dspace/handle/2261/11909%5Cnpapers://8461d6ef-4184-45b2-aa3d-395291ea6525/Paper/p3868) doi: 10.1016/j.epsl.2004.04.016

887 Morales Rivera, A. M., Amelung, F., & Mothes, P. (2016, 7). Volcano deforma-
888 tion survey over the Northern and Central Andes with ALOS InSAR time
889 series. *Geochemistry, Geophysics, Geosystems*, 17(7), 2869–2883. Re-
890 trieved from [https://onlinelibrary.wiley.com/doi/full/10.1002/](https://onlinelibrary.wiley.com/doi/full/10.1002/2016GC006393)
891 [2016GC006393](https://onlinelibrary.wiley.com/doi/full/10.1002/2016GC006393)[https://onlinelibrary.wiley.com/doi/abs/10.1002/](https://onlinelibrary.wiley.com/doi/abs/10.1002/2016GC006393)
892 [2016GC006393](https://onlinelibrary.wiley.com/doi/abs/10.1002/2016GC006393)[https://agupubs.onlinelibrary.wiley.com/doi/10.1002/](https://agupubs.onlinelibrary.wiley.com/doi/10.1002/2016GC006393)
893 [2016GC006393](https://agupubs.onlinelibrary.wiley.com/doi/10.1002/2016GC006393) doi: 10.1002/2016GC006393

894 Moran, S. C., Kwoun, O., Masterlark, T., & Lu, Z. (2006, 2). On the absence of
895 InSAR-detected volcano deformation spanning the 1995–1996 and 1999 erup-
896 tions of Shishaldin Volcano, Alaska. *Journal of Volcanology and Geothermal*
897 *Research*, 150(1-3), 119–131. doi: 10.1016/J.JVOLGEORES.2005.07.013

898 Naismith, A. K., Matthew Watson, I., Escobar-Wolf, R., Chigna, G., Thomas, H.,
899 Coppola, D., & Chun, C. (2019, 2). Eruption frequency patterns through time
900 for the current (1999–2018) activity cycle at Volcán de Fuego derived from
901 remote sensing data: Evidence for an accelerating cycle of explosive paroxysms
902 and potential implications of eruptive activity. *Journal of Volcanology and*

- 903 *Geothermal Research*, 371, 206–219. doi: 10.1016/j.jvolgeores.2019.01.001
- 904 Neal, C. A., Brantley, S. R., Antolik, L., Babb, J. L., & Etc. (2019). The 2018 rift
 905 eruption and summit collapse of Kīlauea Volcano. *Science*, 363(January), 367–
 906 374.
- 907 Ohmoto, H., & Kerrick, D. M. (1977, 10). Devolatilization equilibria in
 908 graphitic systems. *American Journal of Science*, 277(8), 1013–1044. Re-
 909 trieved from <http://www.ajsonline.org/content/277/8/1013> doi:
 910 10.2475/ajs.277.8.1013
- 911 Okada, Y. (1985). *SURFACE DEFORMATION DUE TO SHEAR AND TEN-*
 912 *SILE FAULTS IN A HALF-SPACE* (Vol. 75; Tech. Rep. No. 4). Retrieved
 913 from [http://www.bosai.go.jp/study/application/dc3d/download/](http://www.bosai.go.jp/study/application/dc3d/download/Okada_1985_BSSA.pdf)
 914 [Okada_1985_BSSA.pdf](http://www.bosai.go.jp/study/application/dc3d/download/Okada_1985_BSSA.pdf)
- 915 Papale, P. (1999). Modeling of the solubility of a two-component H₂O + CO₂ fluid
 916 in silicate liquids. *American Mineralogist*, 84(4), 477–492. doi: 10.2138/am-
 917 -1999-0402
- 918 Papale, P., Moretti, R., & Barbato, D. (2006). The compositional dependence of the
 919 saturation surface of H₂O + CO₂ fluids in silicate melts. *Chemical Geology*,
 920 229(1-3), 78–95. doi: 10.1016/j.chemgeo.2006.01.013
- 921 Piochi, M., Bruno, P. P., De Astis, G., Piochi, M., Bruno, P. P., & De Astis, G.
 922 (2005, 7). Relative roles of rifting tectonics and magma ascent processes: In-
 923 ferences from geophysical, structural, volcanological, and geochemical data for
 924 the Neapolitan volcanic region (southern Italy). *Geochemistry, Geophysics,*
 925 *Geosystems*, 6(7). Retrieved from [https://onlinelibrary.wiley.com/doi/](https://onlinelibrary.wiley.com/doi/full/10.1029/2004GC000885)
 926 [full/10.1029/2004GC000885](https://onlinelibrary.wiley.com/doi/abs/10.1029/2004GC000885)[https://onlinelibrary.wiley.com/doi/abs/](https://onlinelibrary.wiley.com/doi/abs/10.1029/2004GC000885)
 927 [https://agupubs.onlinelibrary.wiley.com/doi/](https://agupubs.onlinelibrary.wiley.com/doi/10.1029/2004GC000885)
 928 [10.1029/2004GC000885](https://agupubs.onlinelibrary.wiley.com/doi/10.1029/2004GC000885) doi: 10.1029/2004GC000885
- 929 Plank, T., Kelley, K. A., Zimmer, M. M., Hauri, E. H., & Wallace, P. J. (2013, 2).
 930 Why do mafic arc magmas contain ~4wt% water on average? *Earth and Plane-*
 931 *tary Science Letters*, 364, 168–179. doi: 10.1016/j.epsl.2012.11.044
- 932 Prata, A. J., & Kerkmann, J. (2007, 3). Simultaneous retrieval of volcanic ash and
 933 SO₂ using MSG-SEVIRI measurements. *Geophysical Research Letters*, 34(5).
 934 Retrieved from [https://agupubs.onlinelibrary.wiley.com/doi/full/](https://agupubs.onlinelibrary.wiley.com/doi/full/10.1029/2006GL028691)
 935 [10.1029/2006GL028691](https://agupubs.onlinelibrary.wiley.com/doi/full/10.1029/2006GL028691)[https://agupubs.onlinelibrary.wiley.com/doi/](https://agupubs.onlinelibrary.wiley.com/doi/full/10.1029/2006GL028691)

- 936 [abs/10.1029/2006GL028691https://agupubs.onlinelibrary.wiley.com/](https://agupubs.onlinelibrary.wiley.com/doi/10.1029/2006GL028691)
 937 [doi/10.1029/2006GL028691](https://doi.org/10.1029/2006GL028691) doi: 10.1029/2006GL028691
- 938 Pritchard, M. E., Biggs, J., Wauthier, C., Sansosti, E., Arnold, D. W., Delgado, F.,
 939 ... Zoffoli, S. (2018). Towards coordinated regional multi-satellite InSAR
 940 volcano observations: results from the Latin America pilot project. *Journal of*
 941 *Applied Volcanology*, 7(1). doi: 10.1186/s13617-018-0074-0
- 942 Reath, K., Pritchard, M., Biggs, J., Andrews, B., Ebmeier, S. K., Bagnardi, M., ...
 943 Poland, M. (2020, 1). Using Conceptual Models to Relate Multiparameter
 944 Satellite Data to Subsurface Volcanic Processes in Latin America. *Geochem-*
 945 *istry, Geophysics, Geosystems*, 21(1), 1–26. doi: 10.1029/2019GC008494
- 946 Reath, K., Pritchard, M., Poland, M., Delgado, F., Carn, S., Coppola, D., ...
 947 Bagnardi, M. (2019, 1). Thermal, Deformation, and Degassing Remote
 948 Sensing Time Series (CE 2000–2017) at the 47 most Active Volcanoes in
 949 Latin America: Implications for Volcanic Systems. *Journal of Geophys-*
 950 *ical Research: Solid Earth*, 124(1), 195–218. Retrieved from [https://](https://onlinelibrary.wiley.com/doi/abs/10.1029/2018JB016199)
 951 onlinelibrary.wiley.com/doi/abs/10.1029/2018JB016199[http://](http://doi.wiley.com/10.1029/2018JB016199)
 952 doi.wiley.com/10.1029/2018JB016199 doi: 10.1029/2018JB016199
- 953 Rivalta, E., & Segall, P. (2008). Magma compressibility and the missing source for
 954 some dike intrusions. *Geophysical Research Letters*, 35(4), 1–5. doi: 10.1029/
 955 2007GL032521
- 956 Rust, A. C., & Cashman, K. V. (2011, 11). Permeability controls on expansion and
 957 size distributions of pyroclasts. *Journal of Geophysical Research: Solid Earth*,
 958 116(11). Retrieved from [https://agupubs.onlinelibrary.wiley.com/doi/](https://agupubs.onlinelibrary.wiley.com/doi/full/10.1029/2011JB008494)
 959 [full/10.1029/2011JB008494](https://agupubs.onlinelibrary.wiley.com/doi/full/10.1029/2011JB008494)[https://agupubs.onlinelibrary.wiley](https://agupubs.onlinelibrary.wiley.com/doi/abs/10.1029/2011JB008494)
 960 [.com/doi/abs/10.1029/2011JB008494](https://agupubs.onlinelibrary.wiley.com/doi/abs/10.1029/2011JB008494)[https://agupubs.onlinelibrary.wiley](https://agupubs.onlinelibrary.wiley.com/doi/10.1029/2011JB008494)
 961 [.com/doi/10.1029/2011JB008494](https://agupubs.onlinelibrary.wiley.com/doi/10.1029/2011JB008494) doi: 10.1029/2011JB008494
- 962 Scaillet, B., & Pichavant, M. (2005). A model of sulphur solubility for hy-
 963 drous mafic melts: application to the determination of magmatic fluid com-
 964 positions of Italian volcanoes. *Annals of Geophysics*. Retrieved from
 965 <https://www.earth-prints.org/handle/2122/930>
- 966 Sigmundsson, F., Pinel, V., Grapenthin, R., Hooper, A., Halldórsson, S. A., Einars-
 967 son, P., ... Yamasaki, T. (2020, 12). Unexpected large eruptions from buoyant
 968 magma bodies within viscoelastic crust. *Nature Communications*, 11(1), 1–

- 969 11. Retrieved from <https://doi.org/10.1038/s41467-020-16054-6> doi:
970 10.1038/s41467-020-16054-6
- 971 Spera, F. J. (2000). Physical properties of magma. *Encyclopedia on Volcanoes*. Re-
972 trieved from <https://ci.nii.ac.jp/naid/10015606430>
- 973 Telling, J., Flower, V. J., & Carn, S. A. (2015, 12). A multi-sensor satellite assess-
974 ment of SO₂ emissions from the 2012–13 eruption of Plosky Tolbachik volcano,
975 Kamchatka. *Journal of Volcanology and Geothermal Research*, *307*, 98–106.
976 doi: 10.1016/J.JVOLGEORES.2015.07.010
- 977 Theys, N., Hedelt, P., De Smedt, I., Lerot, C., Yu, H., Vlietinck, J., . . . Van Roozen-
978 dael, M. (2019, 12). Global monitoring of volcanic SO₂ degassing with
979 unprecedented resolution from TROPOMI onboard Sentinel-5 Precur-
980 sor. *Scientific Reports*, *9*(1), 1–10. Retrieved from [www.nature.com/](http://www.nature.com/scientificreports)
981 [scientificreports](http://www.nature.com/scientificreports) doi: 10.1038/s41598-019-39279-y
- 982 Voight, B., Widiwijayanti, C., Mattioli, G., Elsworth, D., Hidayat, D., & Strutt,
983 M. (2010, 10). Magma-sponge hypothesis and stratovolcanoes: Case for
984 a compressible reservoir and quasi-steady deep influx at Soufrière Hills
985 Volcano, Montserrat. *Geophysical Research Letters*, *37*(19), n/a-n/a.
986 Retrieved from <http://doi.wiley.com/10.1029/2009GL041732> doi:
987 10.1029/2009GL041732
- 988 Wallace, P. J. (2001). Volcanic SO₂ emissions and the abundance and distribution
989 of exsolved gas in magma bodies. *Journal of Volcanology and Geothermal Re-*
990 *search*, *108*(1-4), 85–106. doi: 10.1016/S0377-0273(00)00279-1
- 991 Wallace, P. J. (2005, 1). Volatiles in subduction zone magmas: Concentrations and
992 fluxes based on melt inclusion and volcanic gas data. *Journal of Volcanology*
993 *and Geothermal Research*, *140*(1-3), 217–240. doi: 10.1016/j.jvolgeores.2004.07
994 .023
- 995 Wallace, P. J., & Carmichael, I. S. (1992, 5). Sulfur in basaltic magmas. *Geochimica*
996 *et Cosmochimica Acta*, *56*(5), 1863–1874. doi: 10.1016/0016-7037(92)90316-B
- 997 Wallace, P. J., & Carmichael, I. S. (1999, 6). Quaternary volcanism near the Val-
998 ley of Mexico: Implications for subduction zone magmatism and the effects of
999 crustal thickness variations on primitive magma compositions. *Contributions*
1000 *to Mineralogy and Petrology*, *135*(4), 291–314. doi: 10.1007/s004100050513
- 1001 Wallace, P. J., & Gerlach, T. M. (1994, 7). Magmatic vapor source for sulfur dioxide

- 1002 released during volcanic eruptions: Evidence from Mount Pinatubo. *Science*,
 1003 *265*(5171), 497–499. Retrieved from <http://science.sciencemag.org/> doi:
 1004 10.1126/science.265.5171.497
- 1005 Wong, Y., & Segall, P. (2020, 11). Joint Inversions of Ground Deformation, Extrusion
 1006 Flux, and Gas Emissions Using Physics-Based Models for the Mount St.
 1007 Helens 2004–2008 Eruption. *Geochemistry, Geophysics, Geosystems*, *21*(12), 1–
 1008 24. Retrieved from [https://agupubs.onlinelibrary.wiley.com/doi/full/](https://agupubs.onlinelibrary.wiley.com/doi/full/10.1029/2020GC009343)
 1009 [10.1029/2020GC009343](https://agupubs.onlinelibrary.wiley.com/doi/abs/10.1029/2020GC009343)[https://agupubs.onlinelibrary.wiley.com/](https://agupubs.onlinelibrary.wiley.com/doi/abs/10.1029/2020GC009343)
 1010 [doi/10.1029/2020GC009343](https://agupubs.onlinelibrary.wiley.com/doi/abs/10.1029/2020GC009343) doi: 10.1029/2020GC009343
- 1012 Wong, Y., Segall, P., Bradley, A., & Anderson, K. (2017). Constraining the
 1013 Magmatic System at Mount St. Helens (2004–2008) Using Bayesian Inver-
 1014 sion With Physics-Based Models Including Gas Escape and Crystallization.
 1015 *Journal of Geophysical Research: Solid Earth*, *122*(10), 7789–7812. doi:
 1016 10.1002/2017JB014343
- 1017 Woods, A. W., & Huppert, H. E. (2003). On magma chamber evolution during slow
 1018 effusive eruptions. *Journal of Geophysical Research*, *108*(B8), 1–16. doi: 10
 1019 .1029/2002jb002019
- 1020 Yang, X.-M., Davis, P. M., & Dieterich, J. H. (1988, 5). Deformation from inflation
 1021 of a dipping finite prolate spheroid in an elastic half-space as a model for vol-
 1022 canic stressing. *Journal of Geophysical Research: Solid Earth*, *93*(B5), 4249–
 1023 4257. Retrieved from <http://doi.wiley.com/10.1029/JB093iB05p04249>
 1024 doi: 10.1029/JB093iB05p04249
- 1025 Yip, S. T. H., Biggs, J., & Albino, F. (2019, 12). Reevaluating Volcanic Deformation
 1026 Using Atmospheric Corrections: Implications for the Magmatic Sys-
 1027 tem of Agung Volcano, Indonesia. *Geophysical Research Letters*, *46*(23),
 1028 13704–13711. Retrieved from [https://onlinelibrary.wiley.com/doi/](https://onlinelibrary.wiley.com/doi/full/10.1029/2019GL085233)
 1029 [full/10.1029/2019GL085233](https://onlinelibrary.wiley.com/doi/abs/10.1029/2019GL085233)[https://onlinelibrary.wiley.com/doi/abs/](https://onlinelibrary.wiley.com/doi/abs/10.1029/2019GL085233)
 1030 [10.1029/2019GL085233](https://agupubs.onlinelibrary.wiley.com/doi/10.1029/2019GL085233)[https://agupubs.onlinelibrary.wiley.com/doi/](https://agupubs.onlinelibrary.wiley.com/doi/10.1029/2019GL085233)
 1031 [10.1029/2019GL085233](https://agupubs.onlinelibrary.wiley.com/doi/10.1029/2019GL085233) doi: 10.1029/2019GL085233
- 1032 Zhan, Y., Gregg, P. M., Le Mével, H., Miller, C. A., & Cardona, C. (2019, 12). In-
 1033 tegrating Reservoir Dynamics, Crustal Stress, and Geophysical Observations
 1034 of the Laguna del Maule Magmatic System by FEM Models and Data Assim-

1035 ilation. *Journal of Geophysical Research: Solid Earth*, 124(12), 13547–13562.
1036 Retrieved from [https://onlinelibrary.wiley.com/doi/abs/10.1029/](https://onlinelibrary.wiley.com/doi/abs/10.1029/2019JB018681)
1037 2019JB018681 doi: 10.1029/2019JB018681
1038 Zimmer, M. M., Plank, T., Hauri, E. H., Yogodzinski, G. M., Stelling, P., Larsen,
1039 J., ... Nye, C. J. (2010, 12). The role of water in generating the calc-
1040 alkaline trend: New volatile data for aleutian magmas and a new tholei-
1041 itic index. *Journal of Petrology*, 51(12), 2411–2444. Retrieved from
1042 <https://academic.oup.com/petrology/article/51/12/2411/1541257>
1043 doi: 10.1093/petrology/egq062